Solid State Sciences 170 (2025) 108127

Contents lists available at ScienceDirect

Solid State Sciences

journal homepage: www.elsevier.com/locate/ssscie

In-gap electronic states of GeAsSe and SiGeAsSe alloys for selector devices from atomistic simulations☆

Sebastiano Caravati [a], Dario Baratella [a], Paolo Fantini [b], Marco Bernasconi [a],*

[a] Department of Materials Science, University of Milano-Bicocca, Via R. Cozzi 55, I-20125, Milano, Italy
[b] Micron Technology Inc., Via Trento 26, I-20871, Vimercate, Italy

ARTICLE INFO

Keywords:
Selector devices
Selenide glasses
Density functional theory
Molecular dynamics

ABSTRACT

GeAsSe alloys are of interest for application in selector devices in combination with both phase change and resistive memories. In this work, we compute the electronic properties of GeAsSe alloys at several compositions and of a Si-doped GeAsSe alloy within Density Functional Theory (DFT). The analysis of the amorphous models generated by quenching from the melt within DFT molecular dynamics aims at gaining information on in-gap states that are believed to control the functional properties of these alloys exploited in the selector devices, namely the switching threshold voltage, its dependence on the preparation conditions of the amorphous material, and its drift with time. The simulations reveal that localized empty in-gap states (electron traps) are mostly related to homopolar Ge–Ge, As–As and Ge–As bonds, while the most localized filled states (hole traps) are mostly related to Se–Se bonds and are particularly evident in Se-rich compositions.

1. Introduction

Amorphous chalcogenide alloys undergo a reversible electronic transition called ovonic threshold switching (OTS) after Ovshinsky, who discovered this effect in late 60' [1]. In this process, the system transforms from a high-resistive (*off*) to a low-resistive (*on*) states upon application of a voltage exceeding a threshold value V_T [2–4]. This property is exploited in phase change memory (PCM) devices made of telluride alloys that also undergo rapid crystallization above the OTS [5–9]. Selector devices based on OTS materials [3,10] have also been developed in combination with both PCM [11,12] and resistive memories [13]. Recently, it was discovered that the V_T of OTS selectors can also depend on the polarity of the programming pulses. This principle is used to store information in devices called selector only memory (SOM), self-selecting memory (SSM), or Single-chalcogenide X-point Memory (SXM). In these devices, a single chalcogenide film plays the role of both the selector and the memory unit [14–18]. Selenide alloys such as $GeSe_x$ [19] or GeAsSe [20,21] are typically considered for selector applications, as these alloys display the OTS, but do not crystallize. Doping of GeAsSe with Si was also explored in several previous experimental works [17,22,23].

The structural properties of GeAsSe (GAS) alloys have been addressed in several previous experimental papers [24–28] and theoretical works based on density Functional Theory (DFT) calculations [29–33]. However, the nature of the in-gap states that are believed to control the functional properties of OTS materials [3,34] has only rarely been addressed in GAS alloys. Notable exceptions are a recent short report on high throughput DFT screening of materials for SOM devices [35], a joint theoretical and experimental work of a possible explanation of the operation of SOM devices [36], and an earlier DFT work on amorphous models of two particular GeSeAs compositions in which a few in-gap states were assigned to overcoordinated Ge atoms [37].

In this work, we extend the scope of previous theoretical works on GAS by addressing the electronic properties of DFT models of several GAS and Si–GAS amorphous alloys with the aim of gaining information on in-gap states that should control the switching threshold voltage, its dependence on the preparation conditions, and its drift with time.

The article is organized as follows: in the next section we will briefly discuss the main phenomenology of the OTS process to make clear the goal of our study and the methodology we used. Then in Section 3, we will justify our choices on the compositions to be studied. In Section 4, we will provide the computational details and a brief description of the methodology we used. In Section 5.1, we present our results on the structural and electronic properties on GeAsSe alloys, while in Section 5.2 we compare the properties of a particular SiGeAsSe alloy with those of GeAsSe alloys with the same fraction of As and Se. Then, in Section 6 we discuss on a more speculative level the possible

☆ This article is part of a Special issue entitled: 'Computational modelling of materials' published in Solid State Sciences.

* Corresponding author.
E-mail address: marco.bernasconi@unimib.it (M. Bernasconi).

https://doi.org/10.1016/j.solidstatesciences.2025.108127
Received 17 July 2025; Received in revised form 18 October 2025; Accepted 28 October 2025
Available online 31 October 2025
1293-2558/© 2025 The Authors. Published by Elsevier Masson SAS. This is an open access article under the CC BY license (http://creativecommons.org/licenses/by/4.0/).

connection between drift, forming and the composition of the alloy, and finally we present our conclusions in Section 7.

2. Phenomenology of the switching process

In OTS materials, the conductivity is low up to a threshold voltage V_T above which the system turns into the so called *on* state which features a conductivity several orders of magnitude higher than below threshold in the so called *off* state. The process is reversible, and the system turns into an *off* state by decreasing the voltage below threshold (eventually with some hysteresis). This behavior has been experimentally characterized since the late ′60, but a compelling microscopic understanding of this process is still under debate. Several phenomenological models have been proposed over the years to describe the threshold switching, among which we quote the mechanism of (i) filament formation by Adler, Ovshinsky and coworkers [38], (ii) impact ionization and Shockley–Hall–Read recombination [39,40] and (iii) thermal assisted conduction [41,42]. A more recent interpretation of the OTS mechanism is based on a bipolar impact ionization avalanche mechanism [4]. In the presence of a different mobility of electrons and holes, this latter model for OTS is suitable, among other features, to account quantitatively for the S-type Negative Differential Resistance (NDR) behavior measured experimentally [4]. In all these models, the threshold voltage is controlled by the band gap and the presence of localized states in the gap. Due to aging, the band gap increases [43] and the density of in-gap states [44] decreases with time in the amorphous phase. Both these effects concur to a decrease of the leakage current below threshold, i.e. to an increase of the resistance. This drift in the resistance has been extensively studied in phase change materials (see Ref. [45] for a review). A clear correlation between the resistance drift and the increase of the threshold voltage is documented experimentally [46].

In the discussion of our results we follow the Poole-Frenkel model for subthreshold conduction that is usually adopted for the electrical transport in chalcogenides [47]. This model is based on the assumption that most thermally generated holes (electrons) are trapped in localized states, i.e. in hole (electron) traps, that are close to the valence (conduction) mobility edge. The applied electric field promotes the transfer of holes (electrons) from the traps to the valence (conduction) mobile states for low trap densities or a trap-to-trap thermally assisted hopping for high trap densities [47]. The subthreshold conduction depends on the activation energy for this jump and on the density of trapped carrier at thermal equilibrium. This results in an activation energy for the subthreshold conduction which is assigned by the distance of the Fermi level from the mobility edge, lower or upper depending on the type of the majority carriers. Therefore, we will assume that a decrease in the density of localized electronic states inside the gap (traps) and a widening of the mobility gap would both induce an increase of the threshold voltage.

The electronic states in the gap and at the band edges (Urbach tails) are dependent on the preparation conditions of the amorphous samples which would then affect the value of the threshold voltage V_T. These considerations provide an interpretation of two important features of the switching process, namely the forming and drift phenomena. It is known that the as-deposited (asdep) amorphous material has a larger threshold voltage V_{T1} than those measured after the first switch. In the first switch (first fire) the asdep material undergoes structural modifications consisting of the process called forming [48]. After forming, the material switches (second fire) at a lower threshold voltage V_{T2} which remains fairly constant after cycling. The difference between the threshold voltage of the first and second fires $\Delta V_T = V_{T1} - V_{T2}$ is an important parameter which, in general, one would like to minimize. Secondly, the threshold voltage V_{T2} drifts with time towards the value of V_{T1} which can be seen as a process of aging of the material produced after forming. It is believed that in the switching process (in the first and second fires) the system can be brought to temperatures above the glass transition where it should behave as a supercooled liquid phase [49]. The forming process would then correspond to the transformation of an asdep material into an amorphous phase rapidly quenched from the supercooled liquid. Then we might assume that the asdep material is closer to the structure of an ideal glass with an eventual larger gap and lower density of in-gap states and then a larger V_T. The material after forming would instead correspond to a less stable amorphous phase with a smaller electronic gap and a higher density of in-gap states which would then undergo aging due to relaxations towards the more stable ideal glass leading to a drift in V_T. These assumptions mirror the picture of the resistance drift in phase change materials in which the increase of resistance with time is due to the aging of the amorphous phase consisting of relaxation of local defective structures towards a more stable and ideal glass [50]. In this picture, stress release and density change with aging are not relevant [51].

3. Choice of the alloy compositions

We adopt the interpretation of the forming and drift phenomena given above as a starting point for the planning of our atomistic simulations. In particular, we would like to clarify (i) the relationship between the structural features of the amorphous phase and the properties of electronic states at and inside the band gap, (ii) the dependence of these structural features on the preparation conditions of the amorphous phase and (iii) on the composition of the alloy.

To this end, we have generated several models of amorphous GeAsSe alloys by quenching from the melt within DFT molecular dynamics (MD) simulations with different quenching protocols to generate amorphous models with different stability and eventually different distributions of in-gap states.

Amorphous models with different stability were generated by varying the quenching time from the melt (1200 K) to 300 K in the range 120-12 ps. The slow quenched models correspond to a more stable glass that should be closer to the asdep phase before forming which exhibits a larger threshold voltage V_{T1}. The models quenched rapidly would instead be closer to the less stable glasses after forming with a lower threshold voltage V_{T2}. On these bases, the study of the in-gap states and of the band gap for different quenching times and different compositions thus allows us to gain information on the trend of the drift in threshold voltage with the alloy composition. In particular, we associate a larger dependence of the band gap and in-gap states on quenching time with a larger ΔV_T and with a larger drift of V_{T2}.

We started our analysis from a Se-poor composition $Ge_{15}As_{34}Se_{51}$ that can be seen as a Ge-doped As_2Se_3 alloy ($Ge_{15}(As_2Se_3)_{17}$). As we will see in the next sections, since the concentration of Se is not enough to form all the bonds needed for As and Ge, a fraction of "wrong" As–As and Ge–As bonds appear. These bonds are weaker than the most abundant Ge–Se and As–Se bonds and are thus more sensitive to incomplete relaxation that may occur upon a fast cooling from the melt. As we will see later on, these bonds give rise to localized states in the gap and close to the band edge that increase in number by shortening the quenching time. Then, we changed the composition to try to tune the distribution of defect states in the gap. We considered the composition $Ge_{25}(As_2Se_3)_{15}$ ($Ge_{25}As_{30}Se_{45}$) that can also be seen as a Ge-doped As_2Se_3 compound with a larger fraction of Ge. This composition would then display a larger fraction of Ge–As bonds. Then, we considered two alloys along the $GeSe_2$–As_2Se_3 pseudobinary line that are expected to show a lower fraction of wrong bonds due to the presence of a sufficient content of Se to form all the bonds needed by Ge and As atoms. Namely, we generated models of $(GeSe_2)_{25}(As_2Se_3)_5$ ($Ge_{25}As_{10}Se_{65}$) and $(GeSe_2)_{12.5}(As_2Se_3)_{12.5}$ ($Ge_{12.5}As_{25}Se_{62.5}$) alloys. Finally, we considered the $(GeSe)_{25}(As_2Se_3)_{10}$ ($Ge_{25}As_{20}Se_{55}$) alloy on the GeSe–As_2Se_3 pseudobinary line. We thus compared three alloys with the same Ge content (25%) but with a different fraction of Se. On the other hand, starting from the $Ge_{25}As_{30}Se_{45}$ composition we substituted a fraction of Ge with Si to generate a model with composition

$Si_{10}Ge_{15}As_{30}Se_{45}$. The structural properties of $Ge_{12.5}As_{25}Se_{62.5}$ and $Ge_{25}As_{10}Se_{65}$ have been studied also in previous DFT works [30–33], while Ref. [29] reports on a DFT study of $Ge_{21}As_{21}Se_{58}$ which is similar to our composition $Ge_{25}As_{20}Se_{55}$.

4. Computational methods

The amorphous models of the different alloys were generated by quenching from the melt within DFT-MD simulations by using the scheme of Kühne et al. [52] implemented in the CP2K suite of programs [53,54]. We used the generalized gradient approximation (GGA) to the exchange–correlation functional proposed by Becke–Lee–Yang–Parr (BLYP) [55,56] that has been shown to better reproduce the structural properties of liquid and amorphous $GeSe_2$ and GeSe compounds [57, 58] with respect to the most commonly used Perdew–Burke–Ernzerhof (PBE) functional [59]. Norm-conserving Goedecker–Teter–Hutter pseudopotentials [60] with four, five and six valence electrons were adopted for Ge, As and Se, respectively. The Kohn–Sham (KS) orbitals were expanded in a Triple-Zeta-Valence plus Polarization Gaussian-type basis set, while the charge density has been expanded in a plane-wave basis set with a cut-off of 240 Ry to efficiently solve the Poisson equation within periodic boundary conditions using the Quickstep scheme [53, 54]. We used an integration time step of 1.5 fs which is ruled by the ionic dynamics. The same scheme was applied in our previous works on the amorphous phase of telluride alloys [61,62]. In our previous experience with telluride GeTe and $Ge_2Sb_2Te_5$ [63,64], the addition of the van der Waals (vdW) correction á la Grimme [65] has a marginal effect on the structural properties of the amorphous phase once the density is fixed, for example, to the experimental density, as opposed to the case of the more Te-rich $GeTe_4$ alloy [66,67]. Since in selenides the effect of vdW interaction is less important than in telluride and the fraction of Se in our alloys does not exceed 65%, in this our first work on these alloys we neglected vdW corrections.

We considered a cubic supercell containing 300 atoms for all compositions. Brillouin Zone (BZ) integration was restricted to the supercell Γ-point. The size of the cell was assigned by the experimental density taken from Refs. [68] that amounts to: 0.034449 atoms/Å^3 (4.384 g/cm^3) for $Ge_{15}As_{34}Se_{51}$, 0.034133 atoms/Å^3 (4.363 g/cm^3) for $Ge_{25}As_{10}Se_{65}$, 0.034801 atoms/Å^3 (4.425 g/cm^3) for $Ge_{25}As_{20}Se_{55}$, 0.034216 atoms/Å^3 (4.493 g/cm^3) for $Ge_{12.5}As_{25}Se_{62.5}$. The density of the composition $Ge_{25}As_{30}Se_{45}$ of 0.035271 atoms/Å^3 is obtained from the interpolation of three neighboring experimental densities from Ref. [68]. We performed simulations at constant volume according to the picture mentioned above for phase change materials in which stress release and density change with aging are not relevant for resistance drift. After equilibrating the liquid at 1200 K for 15 ps, the system was quenched to 300 K either in 120, 40 or 12 ps generating three different models for each composition. For the single composition $Ge_{15}As_{34}Se_{51}$, we also generated a fourth model with a shorter quenching time of 6 ps. After structural optimization at zero temperature and fixed volume, the residual pressure is below 0.5 GPa in all models. The structural properties of the amorphous models are computed by averaging over a 3 ps trajectory at 300 K. The electronic properties refer instead to the models optimized at zero temperature from the last snapshot of the 300 K simulation. We must admit that three models for each composition are not yet a statistically meaningful set, but still these simulations can provide some hints on the issues outlined in Section 2 as we will see in the next section. This work must be seen as a preliminary investigation in this direction, aimed also at generating a database for the development of machine learning potentials (ML) for these alloys that would allow generating a large number of small (300 atoms) amorphous models at a modest computational cost, to improve the statistics on the in-gap states. This approach has recently been adopted to study in-gap states in some telluride alloys [69].

The electronic density of states (DOS) is computed from KS orbitals at the supercell Γ-point broadened by a Gaussian function with a variance of 41 meV. To quantify the localization properties of individual KS states, we computed the inverse participation ratio (IPR) which is defined for the ith state by $\sum_j c_{ij}^4/\left(\sum_j c_{ij}^2\right)^2$ where j runs over the Gaussian-type orbitals (GTOs) of the basis set, while c_{ij} are the expansion coefficients of the ith KS state in GTOs. According to this definition, the value of the IPR varies from $1/N$ for a completely delocalized KS state where N is the total number of the Gaussian-type orbitals of the basis set, to one for a mode completely localized on a single orbital.

As a proxy of the mobility gap, we computed the Tauc gap [70] which is defined by the intercept with the energy axis of the linear extrapolation of $\omega\sqrt{\varepsilon_2(\omega)}$ as a function of ω, where $\varepsilon_2(\omega)$ is the imaginary part of the dielectric function. In turn, we computed $\varepsilon_2(\omega)$ in the random phase approximation (RPA) from Kohn–Sham (KS) orbitals within DFT

$$\varepsilon_2(\omega) = \frac{8\pi^2}{3V_o\omega^2}\sum_{v,c}|\langle c|\mathbf{p}|v\rangle|^2\delta(\omega - E_c + E_v), \tag{1}$$

where E_c and E_v refer to the energies of conduction and valence bands at the Γ-point of the supercell BZ. V_o is the unit cell volume. In the actual calculation, the δ-functions are substituted by a Gaussian functions with variance of 27 meV. Since the BLYP functional, as all functionals in the Gradient Corrected Approximation (GGA) are known to underestimate the band gap, the electronic properties has been also computed with the hybrid functional of Ref. [71] (HSE) in which exact exchange (Hartree–Fock) is mixed with the Perdew–Burke–Ernzherof GGA functional [59]. This functional was shown to correctly reproduce the band gap and the optical spectra of Te-based alloys (GeTe, GST, Sb_2Te_3) [72,73]. The HSE functional is computationally much more expensive than GGA functionals and thus it was not used in MD simulations but just to compute the electronic structure of models generated with the BLYP functional. To this end, the models first generated and optimized with the BLYP functional have been further optimized with the PBE functional which is closer to the HSE one. The HSE calculations have been performed with PBE pseudopotentials.

5. Results

5.1. Structural and electronic properties of GeAsSe alloys

Before addressing the structural properties of GAS alloys, we recall the crystal structure of the two binary systems GeSe and $GeSe_2$. GeSe crystallizes in an orthorhombic phase (space group *Pnma*) [74]. The crystal is made of GeSe bilayers as shown in Fig. 1a. The atoms are 3-coordinated in a pyramidal configuration due to chemical bonding involving p-orbitals only. The formation energy is 60 kJ/mole and the electronic gap is 1.09 eV [74]. $GeSe_2$ crystallizes instead in a monoclinic phase (space group $P2_1/c$) [75] with an electronic gap of 2.18 eV [76]. The crystal is made of chains of corner- and edge-sharing tetrahedra as shown in Fig. 1b. The formation energy is 115 kJ/mole which is larger than that of the GeSe composition. For $GeSe_x$ alloys the tetrahedra are thus lower in energy than the pyramidal configurations. For comparison, we recall that As_2Se_3 crystallizes in a layered structure (space group $P2_1/c$) consisting of two-dimensional sheets with 2-coordinated Se and 3-coordinated As in a pyramidal geometry [77]. The band gap of crystalline As_2Se_3 is 1.73 eV [76].

5.1.1. Structural properties of GeAsSe alloy

In this section, we discuss the structural properties of the models of amorphous GeAsSe alloys at different compositions generated by quenching from the melt in 120 ps at the experimental density which will be referred to as the mq120 models. As an example, a snapshot of the mq120 model and the partial pair correlation functions (PCFs) for the composition $Ge_{15}As_{34}Se_{51}$ are shown in Fig. 2 and Fig. 3. The

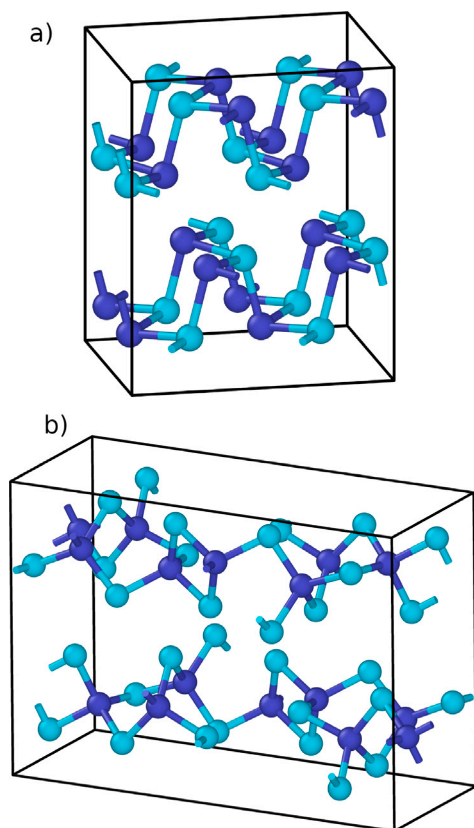

Fig. 1. (a) Crystal structure of GeSe: all atoms are 3-coordinated in a pyramidal configuration. (b) Crystal structure of the monoclinic phase of $GeSe_2$ displaying chains of edge- and corner-sharing $GeSe_4$ tetrahedra. Blue and azure spheres denote Ge and Se atoms.

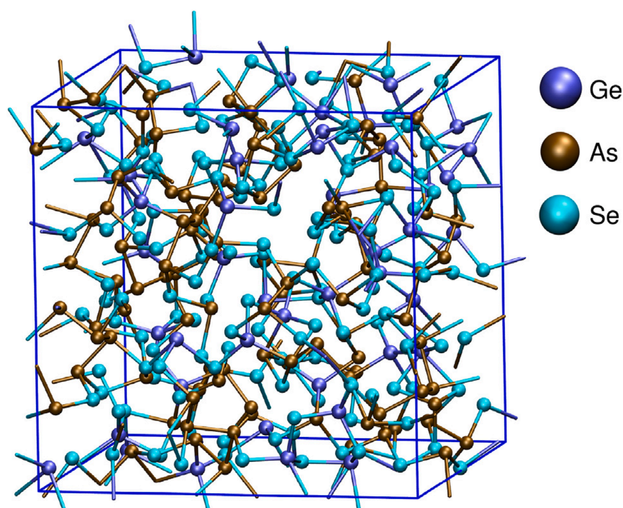

Fig. 2. Snapshot of the mq120 model of a-$Ge_{15}As_{34}Se_{51}$.

cutoff distances which define the formation of a bond are reported in Fig. 3 for each pair.

The PCFs for all compositions and for different quenching times are reported in Figs. S1-S5 in the Supplemental Material (SM). Integration of the partial pair correlation function up to a bonding cutoff provide the average coordination number reported in Table 1. The corresponding data for the models quenched in 40 and 12 ps are collected in Table SI in the SM. The distribution of the coordination numbers for the mq120 models are reported in Fig. 4. The corresponding data for the models quenched in 40 and 12 ps are collected in Figs. S6-S10 in the SM. The percentage of the different types of bonds in the mq120 models is shown instead in Table 2. In Table 2, we also report the estimate of the single bond dissociation energy for homopolar and heteropolar bonds taken from Ref. [76] as obtained from thermochemical data and Pauling electronegativity. In the following, we will refer to weaker or stronger bonds with reference to this table and therefore to a general expectation on the strength of a single bond irrespective to its local environment, length or alloy composition. It is a qualitative hierarchy of the bond strength that we assume to be applicable to our alloys as well. Our results on the partial coordination numbers agree well with previous DFT results [29,31,32,32,33] that are also reported in Table 1. The comparison with the experimental data will be discussed later on.

Note the presence of a significant fraction of As–As bonds in $Ge_{25}As_{30}Se_{45}$ and $Ge_{15}As_{34}Se_{51}$ and a smaller fraction of Ge–As bonds. If we consider the GeAsSe system as a mixture of the GeSe and AsSe

Table 1
Average coordination numbers for different pairs of atoms computed from the partial pair correlation functions for the $Ge_xAs_ySe_{100-x-y}$ models generated by quenching from the melt in 120 ps. Data in parenthesis refer to previous DFT results from Ref. [31] for $Ge_{12.5}As_{25}Se_{62.5}$, Ref. [33] for $Ge_{25}As_{10}Se_{65}$ and Ref. [29] for the composition $Ge_{21}As_{21}Se_{58}$ that is close to our composition $Ge_{25}As_{20}Se_{55}$. The discrepancy between our results and previous DFT data [33] for the same $Ge_{25}As_{10}Se_{65}$ alloy mostly comes from a different choice of the bonding cutoff.

Model	With	Ge	As	Se	Total
$Ge_{25}As_{30}Se_{45}$					
(120 ps)	Ge	0.16	0.44	2.79	3.39
	As	0.37	1.40	1.23	3.00
	Se	1.55	0.82	–	2.37
$Ge_{15}As_{34}Se_{51}$					
(120 ps)	Ge	0.04	0.47	3.00	3.51
	As	0.21	0.94	1.87	3.02
	Se	0.88	1.25	0.07	2.20
$Ge_{25}As_{20}Se_{55}$					
(120 ps)	Ge	0.08 (0.08)	0.19 (0.35)	3.13 (3.37)	3.40
	As	0.23 (0.35)	0.53 (0.65)	2.23 (1.97)	3.00
	Se	1.42 (1.22)	0.81 (0.71)	0.07 (0.12)	2.31
$Ge_{12.5}As_{25}Se_{62.5}$					
(120 ps)	Ge	0.11 (0.02)	0.24 (0.18)	3.34 (3.33)	3.68
	As	0.12 (0.10)	0.13 (0.30)	2.76 (2.63)	3.01
	Se	0.67 (0.65)	1.11 (1.05)	0.29 (0.40)	2.07
$Ge_{25}As_{10}Se_{65}$					
(120 ps)	Ge	0.03 (0.16)	0.03 (0.07)	3.60 (3.11)	3.65
	As	0.07 (0.00)	0.07 (0.18)	2.87 (2.87)	3.00
	Se	1.38 (1.20)	0.44 (0.44)	0.37 (0.57)	2.19

Table 2
Percentage of different types of bonds and ratio between the fraction of Ge atoms and Se atoms for the models of GeAsSe alloys at different compositions quenched in 120 ps from the melt. Bond energies in kcal/mol from Ref. [76] are given in the last column.

Bonds type	$Ge_{25}As_{30}Se_{45}$	$Ge_{15}As_{34}Se_{51}$	$Ge_{25}As_{20}Se_{55}$	$Ge_{12.5}As_{25}Se_{62.5}$	$Ge_{25}As_{10}Se_{65}$	Bond energy
	%					(kcal/mol)
As–Se	26	48	33	55	22	41.7
Ge–Se	49.5	34	58	33	68	49.1
As–As	15	12	4	1.3	0.3	32.1
Ge–As	8	5	3	2	0.5	35.8
Ge–Ge	1.4	0.3	0.7	0.5	0.3	37.6
Se–Se	–	1	1.5	7	9	44.0
%Ge/%Se	0.56	0.29	0.46	0.2	0.39	

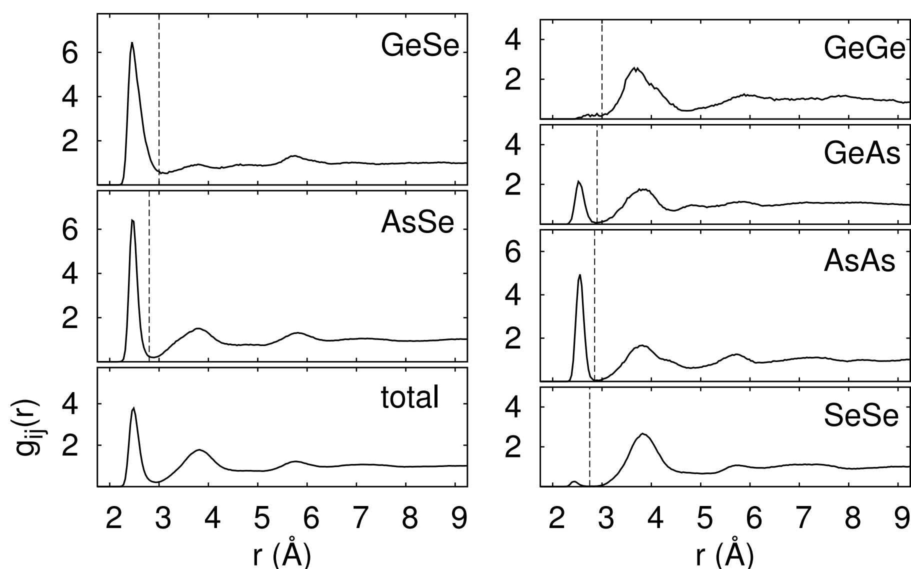

Fig. 3. Partial pair correlation functions of the mq120 model of a-$Ge_{15}As_{34}Se_{51}$. The dashed vertical lines indicate the cutoff used to define the formation of a bond, namely 3.0 Å (Ge–Se), 2.8 Å (As–Se), 3.0 Å (Ge–Ge), 2.9 Å (Ge–As), 2.8 Å (As–As), and 2.8 Å (Se–Se).

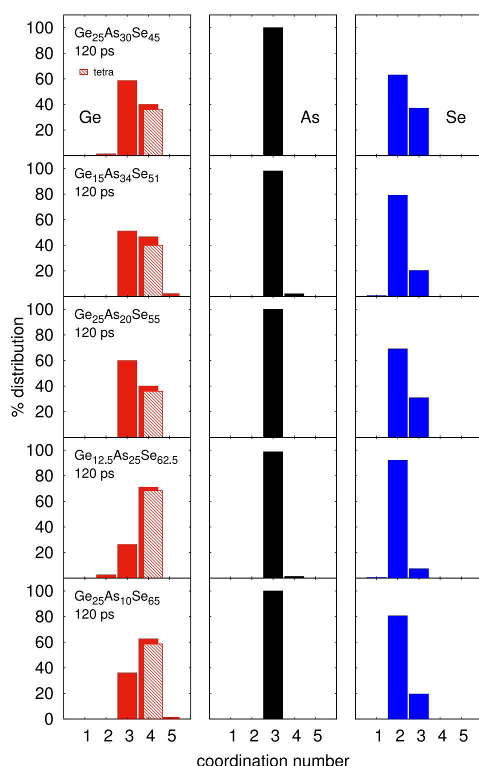

Fig. 4. Distribution of coordination numbers of different models of amorphous GeAsSe alloys quenched in 120 ps from the melt.

binaries, we should see the As–As, Ge–As, Se–Se and Ge–Ge bonds are "wrong" bonds, weaker than the main Ge–Se and As–Se bonds which are responsible for most of the cohesive energy and for the formation energy of the two binaries. Since the two compositions $Ge_{25}As_{30}Se_{45}$ and $Ge_{15}As_{34}Se_{51}$ correspond to Ge-doped As_2Se_3 alloys and Ge is mostly bound to Se, a fraction of As atoms has no Se atoms to bond to, which results in the formation of As–As bonds. The fraction of "wrong", homopolar As–As and Ge–Ge bonds increases with increasing the Ge content in $Ge_x(As_2Se_3)_{1-x}$ alloys. On the other hand, the fraction of wrong As–As bonds is low for the other three compositions that lye on the pseudobinary lines $(GeSe_2)_x(As_2Se_3)_{1-x}$ or $(GeSe)_x(As_2Se_3)_{1-x}$ where the fraction of Se is sufficient to saturate most of the bonds with both Ge and As atoms.

We can then make several comments on Table 2 regarding the dependence of the different bonding types as a function of composition which is in line with previous DFT works [30–33]: (i) the majority of bonds are the stronger Ge–Se and As–Se bonds, (ii) the fraction of wrong Ge–Ge bonds is always negligible, (iii) the fraction of As–As and Ge–As wrong bonds is a monotonic decreasing function of the Se content, (iv) the fraction of Se–Se wrong bonds is a monotonic increasing function of the Se content.

Concerning the local bonding geometry, Se atoms are mostly 2-coordinated with a minority of 3-coordinated atoms; As atoms are nearly always 3-coordinated; Ge atoms are 3- or 4-coordinated with a very few 5-coordinated atoms. Snapshots of the local bonding geometry corresponding to the different coordination are given in Fig. 5 which also shows isosurfaces of the Wannier Functions (WFs). The WFs are the periodic version of the Boys orbitals obtained by the unitary transformation of the occupied KS orbitals that minimizes the quadratic spread [78]; they give a vivid picture of the type of bonding.

The large majority of 4-coordinated Ge atoms corresponds to a tetrahedral bonding geometry with sp^3 hybridization (see Fig. 5a). A small fraction of 4-coordinated Ge atoms are in a defective octahedral geometry with bonding angles of 90° due to the formation of bonds with p orbitals only (see Fig. 5d). The fourth bond is longer than the other three as occurs, for instance, in $Ge_2Sb_2Te_5$ [79–81]. 3-coordinated Ge and As atoms are in a pyramidal geometry with bonding angles of 90° which involves only p orbitals (see Fig. 5b–c). In the defective octahedral and pyramidal configurations, the s electrons form a lone pair, visible as a spherical WF in Fig. 5b–d. The 2-coordinated Se atoms form two covalent bonds with p orbitals at ∼90° and display a p lone pair and a s lone pair (see Fig. 5e). Since Ge has only two p electrons, a dative bond from a p-type lone pair of Se is needed to close the p shell. The Se atoms donating a dative bond to Ge atoms become 3-coordinated. The presence of dative bonds from chalcogen atoms is similar to what occurs in the GeSbTe compounds [61,80–82].

To quantify the fraction of tetrahedra, we used the local order parameter q introduced in Ref. [83] as an indicator of the tetrahedricity of the bonding geometry. It is defined by $q = 1 - \frac{3}{8}\sum_{i>k}(\frac{1}{3} + \cos\theta_{ijk})^2$ where the sum runs over the pairs of atoms bonded to a central atom

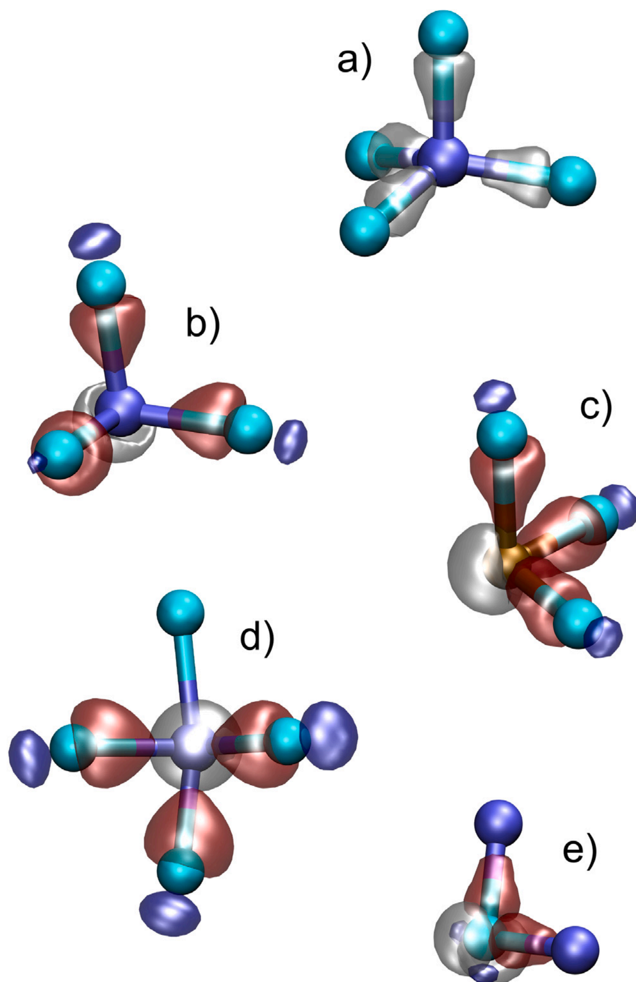

Fig. 5. Isosurface of Wannier functions for (a) Ge in a tetrahedral site, (b) Ge and (c) As in a pyramidal bonding geometry, (d) Ge in defective octahedra with coordination four and (e) Se 2-coordinated. Isosurfaces with different colors (red and blue) have different sign. Wannier functions with spherical isosurfaces (gray) are *s*-type lone pairs. Blue, azure and brown spheres denote Ge, Se and As atoms.

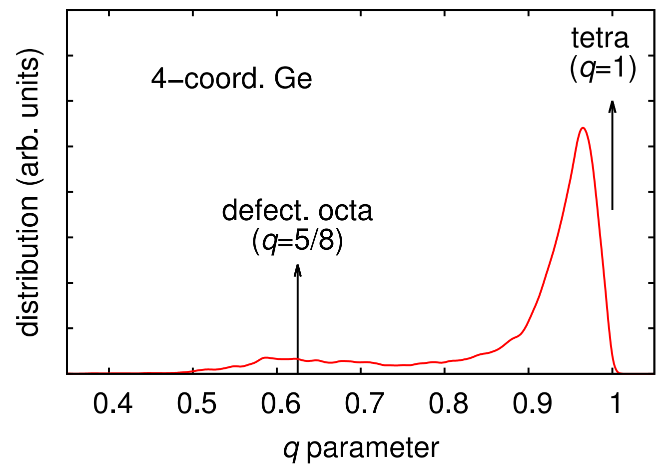

Fig. 6. Distribution of the local order parameter q for tetrahedricity (see text) for 4-coordinated Ge atoms in the mq120 model of $Ge_{15}As_{34}Se_{51}$. Vertical lines indicate the values of q for selected ideal geometries.

j and forming a bonding angle θ_{ijk}. The order parameter is $q = 1$ for the ideal tetrahedral geometry, $q = 0$ for the 6-coordinated octahedral site, and $q = 5/8$ for a 4-coordinated defective octahedral site. As an example, we show in Fig. 6 the distribution of the q order parameter for 4-coordinated Ge atoms in $Ge_{15}As_{34}Se_{51}$ that clearly feature a dominant peak corresponding to tetrahedra with a broad tail due to distorted defective octahedra. The integration of the q-order parameter from about 0.8 to 1.0 gives a measure of the fraction of tetrahedra, as we have shown in a previous work [62]. This number is consistent with the fraction defective octahedral/pyramidal configurations with only p-type bonding orbitals that can be obtained by looking at Ge atoms with a s-like WF [80].

The fraction of tetrahedral Ge and the distribution of the different types of tetrahedra for the different compositions and the different quenching times are compared in Table 3. The tetrahedra can be isolated, corner- or edge-sharing. Corner-sharing tetrahedra are actually more stable than edge-sharing ones. In fact, structural relaxations leading to the transformation of edge-sharing in corner sharing tetrahedra are well documented in $GeSe_x$ alloys [84]. However, it is unknown whether these structural relaxations might have some impact on the transport properties and thus on the threshold switching. The relaxation might involve states deeper in the valence band that do not affect the electrical conductivity. Anyway, for the compositions studied here, the fraction of tetrahedral Ge atoms involved in edge-sharing tetrahedra is at most 10 % compared to a fraction of about 50% in $GeSe_2$ [85].

The fraction of Ge atoms in a tetrahedral coordination increases by decreasing the ratio between the fraction of Ge and Se atoms (%Ge/%Se in Table 2) with an exception for the composition $Ge_{15}As_{34}Se_{51}$ that has a lower fraction of tetrahedra with respect to composition $(GeSe_2)_{25}(As_2Se_3)_5$, although it has a lower %Ge/%Se ratio. Moreover, the fraction of tetrahedra is maximal for compositions along the pseudobinary line $GeSe_2$–As_2Se_3.

Information on the bonding geometry is obtained also from the bond angle distribution functions resolved for the different species in Fig. 7 for the composition $Ge_{15}As_{34}Se_{51}$. The distribution is clearly peaked at around 90°–100° for all atoms, but for tetrahedral Ge atoms whose angles distribution is peaked instead at about 109° as expected. The tail of the distribution at higher angles for octahedral Ge is due to 4-coordinated atoms in defective octahedra forming ideally an angle at 180° (see Fig. 5c). The Ge–Se bond length in tetrahedra is shorter than in octahedra as shown in Fig. S11 in SM reporting the Ge–Se pair correlation function resolved for the two different types of bond for the mq120 model of a-$Ge_{25}As_{20}Se_{55}$. This alloy has a low fraction of tetrahedra (see Table 3) but a large Ge–Se coordination number (compared with other compositions with a similar fraction of tetrahedral Ge, see Tables 1 and 3) which means that this alloy features a larger fraction of Ge–Se octahedral longer bonds responsible for the shoulder in the Ge–Se pair correlation function which is more evident for this composition than for others (see Fig. S3 in the SM).

In summarizing our results on the structural properties, as we have already mentioned, the partial coordination numbers are very close to previous DFT works for alloys with the same or similar compositions (see Table 1). In particular, the DFT-BLYP model with composition $Ge_{21}As_{21}Se_{58}$ of Ref. [29], whose partial coordination numbers are very similar to our $Ge_{25}As_{20}Se_{55}$ model, reproduces well the experimental total structure factor from x-ray and neutron diffraction [29]. This model has, however, a much lower fraction of homopolar bonds (Ge–Ge and As–As) than the model obtained from a Reverse Monte Carlo (RMC) fitting of the experimental x-ray diffraction (XRD) and extended x-ray absorption fine structure (EXAFS) data in Ref. [28]. Similarly, the fractions of As–As and Ge–Ge homopolar bonds in our models at the other compositions are systematically much lower than those of the RMC models fitted on experimental data in Ref. [28] and in other works by the same group [24,25,27]. We compare the partial coordination numbers of our and previous DFT models with those of the RMC models

Table 3
Statistics of Ge atoms in tetrahedral environment (Ge_t) in the mq120 models.

Composition	Ge_t (%)	abs. number	Ge_t with wrong bonds	Isolated Ge_t	corner sh. couples	edge sh. couples
$Ge_{25}As_{30}Se_{45}$	36	27	25	9	15	0
$Ge_{15}As_{34}Se_{51}$	40	18	11	11	5	0
$Ge_{25}As_{20}Se_{55}$	36	27	16	8	11	1
$Ge_{12.5}As_{25}Se_{62.5}$	68	26	11	14	5	2
$Ge_{25}As_{10}Se_{65}$	57	43	3	6	24	3
$Si_{10}Ge_{15}As_{30}Se_{45}$	35	26	24	11	7	3

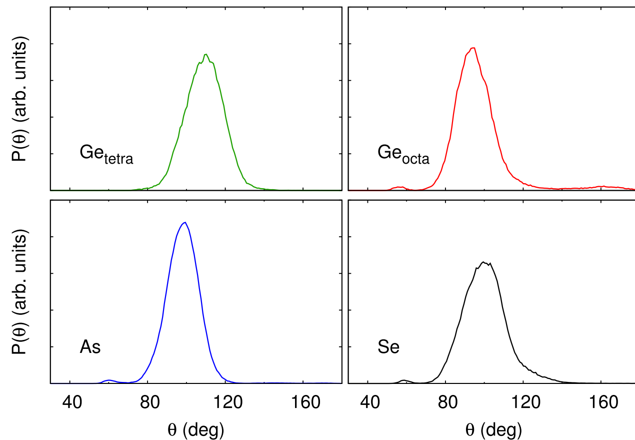

Fig. 7. Bond angles distribution function resolved for the different species in the mq120 model of $Ge_{15}As_{34}Se_{51}$. Tetrahedral Ge atoms are identified by a q order parameter larger than 0.8 (see text). The small feature at 60° is due to a As–Se-Ge 3-membered ring.

from Refs. [24,28] in Table SII in the SM. Our theoretical structure factor $S(q)$ with x-ray atomic form factors is compared with XRD experimental data of similar compositions, when available, in Fig. S12 in the SM. For composition $Ge_{15}As_{34}Se_{51}$ we also compare our total pair correlation function with the experimental data obtained by the Fourier transform of the structure factor in Ref. [24] in Fig. S12 in the SM. There is clearly room for improvements, but it is unclear whether the discrepancy in the partial coordination numbers with experiments arises from the misfits in the $S(q)$ or from inaccuracies in the RMC which are generated by fitting diffraction data with no information on the underlying potential energy surface. We also mention that in the RMC analysis the total coordination number was initially fixed at 4, 3, 2 for Ge, As and Se atoms, and then relaxed in the final stage of the fitting [24,27,28]. We must also note that the diffraction and EXAFS data refer to as-deposited samples, while our models are generated by a fast quenching from the melt that, anyway, are expected to be closer to the material in the device after cycling. Naively, we would expect that the asdep material should be closer to the ideal glass and then, as opposed to the RMC models, feature a lower fraction of wrong bonds than our models very rapidly quenched from the melt. In fact, a more recent RCM fitting of EXAFS data for the composition $Ge_{6.25}As_{32.5}Se_{61.25}$ yielded a much lower content of As–As and Ge–Ge homopolar bonds than the DFT model generated by quenching from the melt by the same authors [32], which in turn had yet a lower content of As–As and Ge–Ge homopolar bonds than the previous RMC model with a similar $Ge_5As_{30}Se_{65}$ composition of Ref. [24]. The high fraction of homopolar As–As and Ge–Ge bonds of the RMC models in Refs. [24,28] has also been questioned by Raman and nuclear magnetic resonance measurements in Ref. [26]. In Table SIII in the SM, we also compare the position of the first peak of the partial correlation functions of our models with previous DFT results and with RMC models. Our bond lengths are systematically slightly longer than the experimental ones from the RMC models. The bonds involving Ge in our models are also slightly longer than those of previous DFT results (see Table SIII in the SM).

We may now wonder how the quenching time might affect the structural properties of the amorphous models. Actually, very little changes can be found by looking at an integrated quantity like the partial pair correlation functions. These are shown in Fig. 8 for the three models quenched from the melt in 120 ps, 40 ps (mq40) or 12 ps (mq12) for $Ge_{15}As_{34}Se_{51}$. Note that the total energy of the different models is higher than that of the model quenched more slowly (120 ps). Namely, the total energies with respect to the mq120 model (120 ps) which is set to zero are: 3 meV/atom (mq40) and 20 meV/atom (mq12). Still, as we will see in the next section, shorter quenching times lead to the formation of a larger number of in-gap localized states.

For all compositions, we observe a very small increase in the overall fraction of As–As, Ge–As and Ge–Ge wrong bonds by decreasing the quenching time (see Fig. S13 and Table SIV in the SM) for all the compositions studied. In the Se-rich $Ge_{25}As_{10}Se_{65}$ and $Ge_{12.5}As_{25}Se_{62.5}$ alloys we observe instead a more pronounced increase of the Se–Se bonds by decreasing the quenching time and a concomitant decrease in the fraction of tetrahedra (see Table SV in the SM). The distribution of the different types of environment for the Se-poor $Ge_{25}As_{30}Se_{45}$ alloy quenched in 40 ps or 12 ps are given in Table SVI and SVII in the SM. In the next section, we discuss how these structural features have an impact on the electronic properties and their dependence on composition and quenching time.

5.1.2. Electronic properties of GeAsSe alloys

The effect of composition and quenching time on the electronic properties of the GeAsSe alloys has been addressed by computing the electronic density of state (DOS) and the optical Tauc gap. The electronic DOS (HSE functional) for the different compositions and quenching time are shown in Fig. 9. As an example, we report the function $\varepsilon_2(\omega)$ and the Tauc plot for the $Ge_{15}As_{34}Se_{51}$ alloy in Fig. S14 in the SM. The Tauc gap for the different compositions and quenching times is reported in Table 4 as obtained from the linear fit of Tauc plots shown in Fig. S15 in the SM. The experimental Tauc gap of $Ge_{25}As_{15}Se_{60}$ is 1.37 eV [86] which compares reasonably well with theoretical values of 1.2 and 1.29 eV for $Ge_{25}As_{20}Se_{55}$ and $Ge_{25}As_{10}Se_{65}$ compositions (see Table 4). Similarly, the experimental Tauc gap of $Ge_{10.5}As_{23.5}Se_{66}$ is 1.45 eV [87], which is close to the theoretical value of 1.38 eV for $Ge_{12.5}As_{25}Se_{62}$.

We can observe that the band gap in the DOS and the Tauc gap (see Table 4) clearly decrease by reducing the quenching time for the two Se-poor compositions $Ge_{15}As_{34}Se_{51}$ and $Ge_{25}As_{30}Se_{45}$. In-gap states close to the band edge or deep in the gap appear by decreasing the quenching time. These states turn out to be mostly localized on Ge–As bonds. This effect is more pronounced for the composition richer in Ge, as expected. The band gap of the DOS and the optical Tauc gap are instead very weakly dependent on the quenching time for the Se-rich alloy $Ge_{25}As_{10}Se_{65}$ on the pseudobinary line $GeSe_2$–As_2Se_3. The situation is intermediate for $Ge_{25}As_{20}Se_{55}$ on the GeSe–As_2Se_3 pseudobinary line that shows a weak dependence of the gap on the quenching time but still the presence of localized states close to the band gap due to Ge–As bonds. The composition $Ge_{12.5}As_{25}Se_{62.5}$ deserves a separate discussion reported later on. Regarding the nature

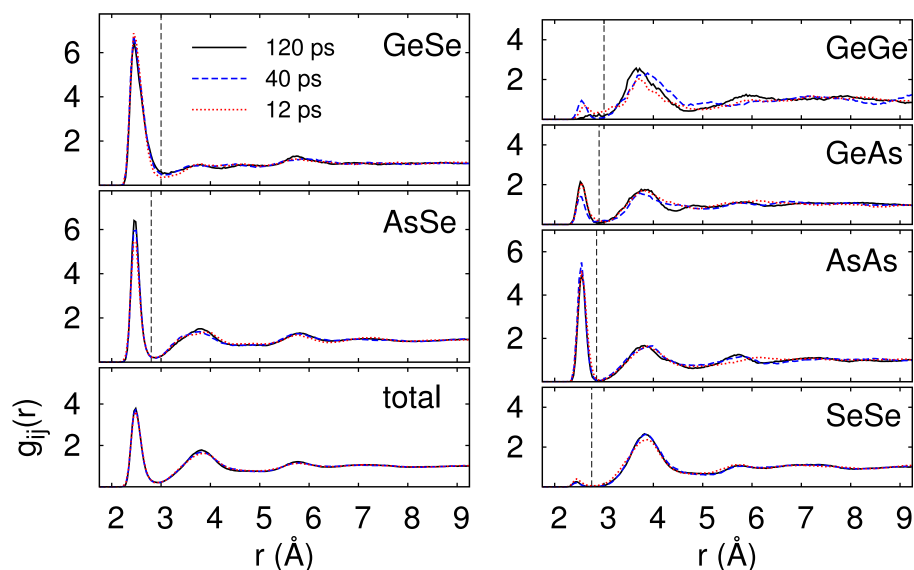

Fig. 8. Partial pair correlation functions of the models of a-$Ge_{15}As_{34}Se_{51}$ generated with different quenching times (120, 40, and 12 ps).

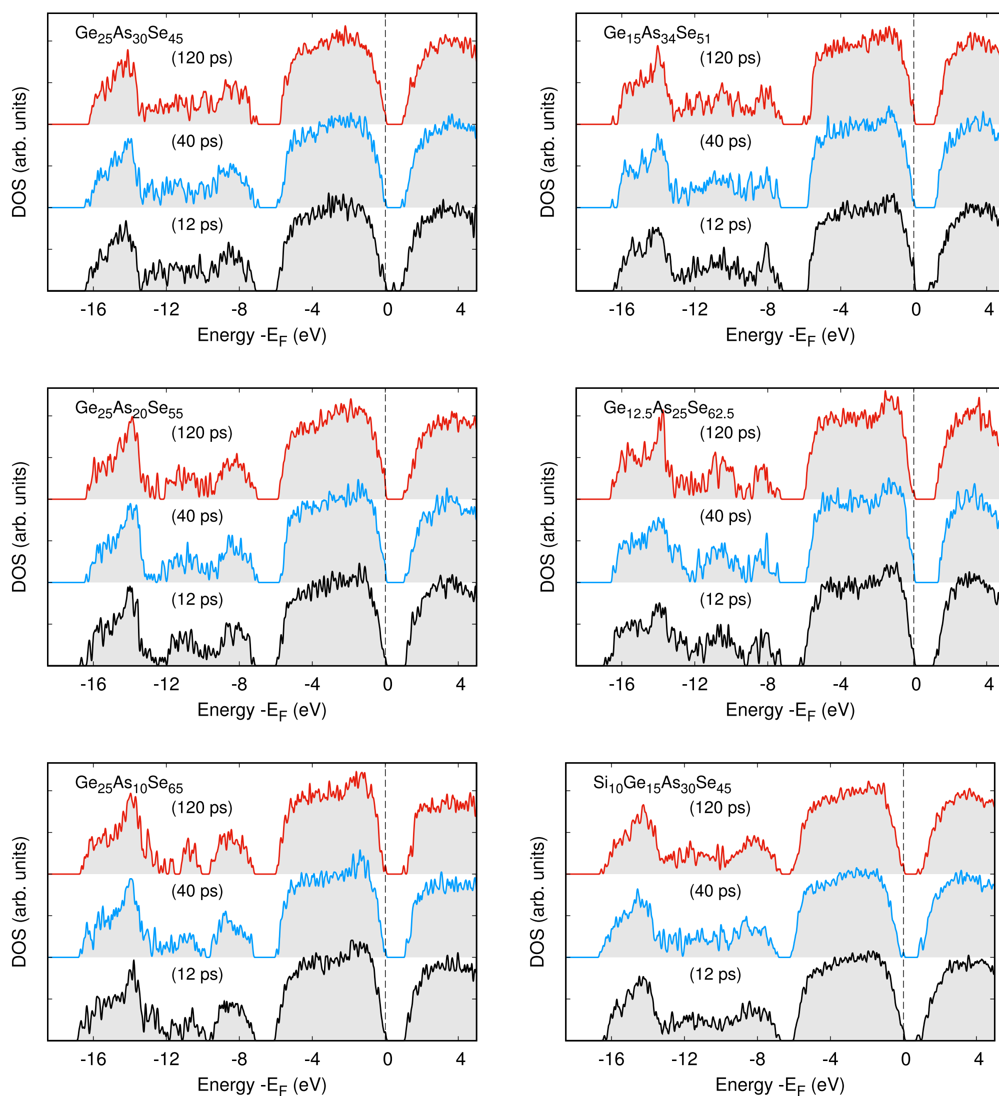

Fig. 9. Electronic density of states of different models of GeAsSe and SiGeAsSe alloys (HSE functional). The zero of energy is the highest occupied KS state (or using a slightly improper nomenclature for a solid, the highest occupied molecular orbital, HOMO).

Table 4
Fraction of Ge atoms in tetrahedral environment (Ge_t) and optical Tauc gap of amorphous models of GeAsSe and SiGeAsSe alloys generated by quenching from the melt with different quenching times.

Model	Alloy type	τ_q (ps)	Ge_t	Optical gap (eV)
$Ge_{25}As_{30}Se_{45}$	$(Ge)_{25}(As_2Se_3)_{15}$	120	36%	1.09
		40	23%	1.12
		12	33%	0.94
$Ge_{15}As_{34}Se_{51}$	$(Ge)_{15}(As_2Se_3)_{17}$	120	40%	1.25
		40	44%	1.27
		12	49%	1.06
		6	40%	1.13
$Ge_{25}As_{20}Se_{55}$	$(GeSe)_{25}(As_2Se_3)_{10}$	120	36%	1.20
		40	43%	1.26
		12	36%	1.22
$Ge_{12.5}As_{25}Se_{62.5}$	$(GeSe_2)_{12.5}(As_2Se_3)_{12.5}$	120	68%	1.38
		40	63%	1.30
		12	32%	1.24
$Ge_{25}As_{10}Se_{65}$	$(GeSe_2)_{25}(As_2Se_3)_5$	120	59%	1.29
		40	49%	1.29
		12	41%	1.27
$Si_{10}Ge_{15}As_{30}Se_{45}$	$(Si)_{10}(Ge)_{15}(As_2Se_3)_{15}$	120	35%	1.23
		40	28%	1.13
		12	36%	1.10

of in-gap states, as an example, we show in Fig. 10 a zoom of the DOS and IPR close to the band gap for the mq120 and mq12 models of $Ge_{15}As_{34}Se_{51}$. The states close to the band edges and inside the band gap are clearly localized. In the mq12 model, the LUMO (lowest unoccupied molecular orbital), LUMO+1 and LUMO+2 are strongly localized on Ge–As bonds for Ge 4-coordinated in a Ge–As_3Se configuration (see Fig. 10). In the mq120 model, the LUMO+1 state is localized on a corner-sharing Ge tetrahedra, while the LUMO and LUMO+2 correspond to Valence Alternation Pairs (VAPs). The VAPs are typical of amorphous chalcogenides and can be seen as originating from two undercoordinated atoms that exchange an electron and then interact with lone pairs of neighboring chalcogens [88,89]. A picture of the formation of a VAP in an AsSe compound is depicted in Fig. 11. The ideal breaking of a As–Se bond gives rise to two radicalic undercoordinated atoms. This configuration is unstable with respect to an electron transfer from As to Se which generates a positively charged As and a negatively charged Se. The Se atom acts as a negative Hubbard-U center and displays two p lone pairs. The undercoordinated, positively charged As atom recovers the 3-coordination by receiving a dative bond from a lone pair of another neighboring Se atom. In alloys with Ge, the negatively charged Se atom of the VAP can also donate one or both of its two p lone pairs to neighboring Ge atoms. These processes lead to the formation of a second 3-coordinated Se atom. In the presence of Ge, the 3-coordinated Se atoms bonded with Ge atoms are part of the network and should not be seen as defects. The corresponding electronic states are thus expected to fall inside the bands. In contrast, 3-coordinated Se bonded with As atoms only can be seen as part of VAPs and they can possibly give rise to localized states at the band edges. This is the case for the LUMO state of the mq120 model depicted in Fig. 10 and the LUMO+2 state as well (not shown). These states are empty (electron traps) and localized on Se–As bonds of two different Se–As_3 centers. In the mq120 model, the localized HOMO state (hole trap) involves a Ge–Ge bond (see Fig. 10).

We remark that, while the amorphous models are semiconducting, the liquid phase is metallic, as shown in Fig. S16 in the SM that compares the DOS of the mq120, mq12 and liquid models of $Ge_{15}As_{34}Se_{51}$. As an example, for this particular composition we also show the projections of the DOS of the mq120 model on different atomic orbitals (s and p) in Fig. 12 and the IPR superimposed to the DOS over the whole spectral range in Fig. S17 in the SM.

A zooming of the DOS and IPR close to the band gap is shown in Figs. 13 and 14 for other two representative compositions of Se-poor $Ge_{25}As_{30}Se_{45}$ alloy and Se-rich $Ge_{25}As_{10}Se_{65}$ alloy with the same Ge content. The corresponding plots for the other compositions are shown in Figs. S18-S22 in the SM. The shortening of the quenching time in the Se-poor $Ge_{25}As_{30}Se_{45}$ alloy gives rise to an in-gap state localized on a Ge–As bond (see Fig. 13 for the assignment of the character of the most localized states). In the slow quenched model the LUMO is a VAP state and the HOMO is localized on a Se–Se bond. In the Se-rich alloy the band gap does not change by shortening the quenching time, albeit states mostly localized on Se–Se bonds are present at the conduction and valence band edges. At the edge of the conduction band, we also observe states localized on tetrahedral Ge atoms (see Fig. 14 for the assignment of the character of the most localized states).

We remark that by decreasing the quenching time the fraction of wrong Ge–As bonds does not change sizably. However, these bonds are weaker than the others and are thus more sensitive to an incomplete relaxation occurring on a short quenching time that gives rise to in-gap states. The Ge–As bonds in Se-poor alloys are thus expected to give rise to a strong drift. In contrast, the states due to Se–Se bonds in Se-rich alloys, albeit also localized at the band edges, seem less sensitive to the quenching time possibly because of the higher strength of Se–Se bonds with respect to Ge–As bonds. The strength of the different types of bonds is reported in Table 2 (from Ref. [76]). Overall, the electron traps, i.e. empty states either deep or close to the conduction band, are mostly due to wrong bonds involving cations (Ge–As) in Se-poor alloys which is in line with previous DFT results on $GeSe_x$ alloys (see for instance Ref. [90]). In contrast, hole traps in our models, i.e. filled states close to the valence band, are mostly due to Se–Se bonds, especially for Se-rich compositions.

The composition $Ge_{12.5}As_{25}Se_{62.5}$ deserves a separate discussion. The localized states at both the valence and conduction edges are mostly localized on Se–Se bonds (see Fig. S21 in the SM). Although the Urbach tails (slope of the Tauc plot [43]) do not appear to change significantly with the quenching time (see Fig. 9 and Fig. S15 in the SM), the Tauc gap decreases by about 0.14 eV (see Table 4) by shortening the quenching time from 120 ps to 12 ps. We can ascribe this change to the large decrease in the fraction of Ge atoms in tetrahedral geometry from 68% (120 ps) to 32% (12 ps). In fact, the band gap of crystalline $GeSe_2$ made of tetrahedra (2.18 eV) is much larger than that of the GeSe crystal (1.09 eV) made of pyramidal configurations. Since tetrahedra are lower in energy than pyramids or defective octahedra, we expect a pyramids/octahedra → tetrahedra transformation upon aging which might thus be another source of resistance drift. This effect might be milder than the structural relaxations involving Ge–As bonds as the Ge–Se bonds in tetrahedra are stronger than Ge–As bonds (see Table 2). Partially substituting Ge with other elements that form only tetrahedra, e.g. Si or Ga, would minimize the drift associated with pyramids → tetrahedra transformation. To address this issue, we generated models of a Si-doped GeAsSe alloy as discussed in the next section.

5.2. Structural and electronic properties of SiGeAsSe alloys

In the following, we report the analysis of the structural and electronic properties of amorphous models (500 atoms at density of 0.03527 atom/Å^3) of the $Si_{10}Ge_{15}As_{30}Se_{45}$ alloy which features the same As and Se content of the $Ge_{25}As_{30}Se_{45}$ alloy discussed in the previous sections. Doping of GeAsSe with Si was explored in several previous experimental works [17,22,23]. The partial pair correlation function is shown in Fig. 15, while the distribution of coordination numbers of models generated with different quenching times from the melt is shown in Fig. 16. The fraction of Ge atoms in tetrahedral configurations and the number of different types of tetrahedra are compared with those of GeAsSe alloys in Table 3. Si atoms are always in the tetrahedral configuration.

The average partial coordination numbers for the different species and different quenching times are given instead in Table 5. The percentage of different types of bonds is compared with that of $Ge_{25}As_{30}Se_{45}$ alloy in Table 6.

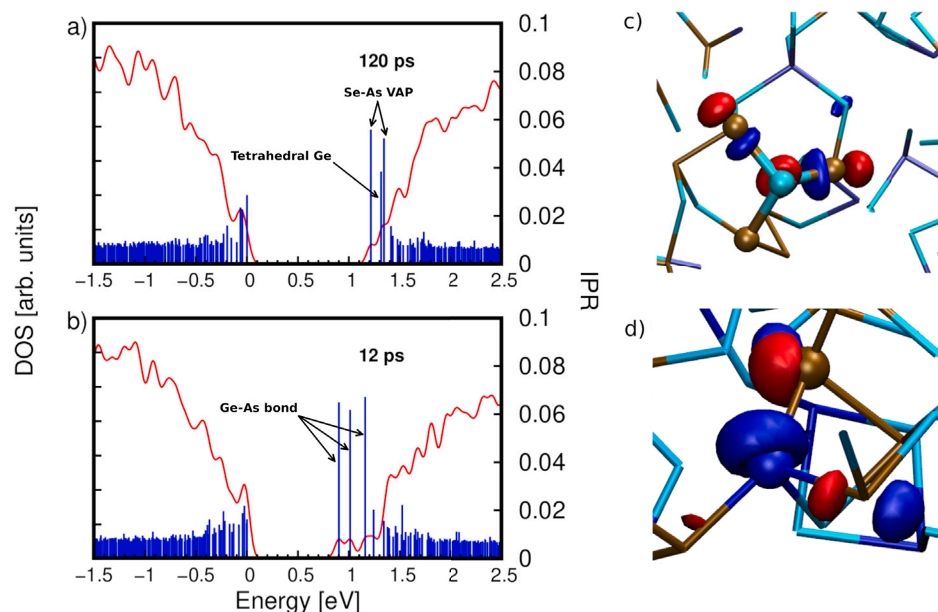

Fig. 10. A zooming of the DOS close to the band gap and the values of the Inverse Participation Ratio (IPR, right scale) are shown for the (a) mq120 and (b) mq12 models of $Ge_{15}As_{34}Se_{51}$. The higher the IPR value the more localized is the individual Kohn–Sham state. The character of the most localized states is indicated in the figure. The LUMO+1 state of the mq120 model is localized on a corner-sharing Ge tetrahedra. (c) A picture of the isosurfaces of the LUMO (lowest unoccupied molecular orbital) in the mq120 model. The isosurface corresponds to half of the maximum value of the KS orbital evaluated on a uniform grid. The LUMO is localized on Se–As_3 center and corresponds to an antibonding, empty state of a Valence Alternation Pair (VAP) defect. The LUMO+2 is another VAP state localized on a different center. Blue, azure and brown spheres denote Ge, Se and As atoms. (d) The LUMO state of the mq12 model which is strongly localized on a Ge–As bond of a 4-coordinated Ge atom in a Ge–As_3Se configuration. The LUMO+1 and LUMO+2 states are localized on a Ge–As_2Se_2 and Ge–$AsSe_3$ groups (HSE functional).

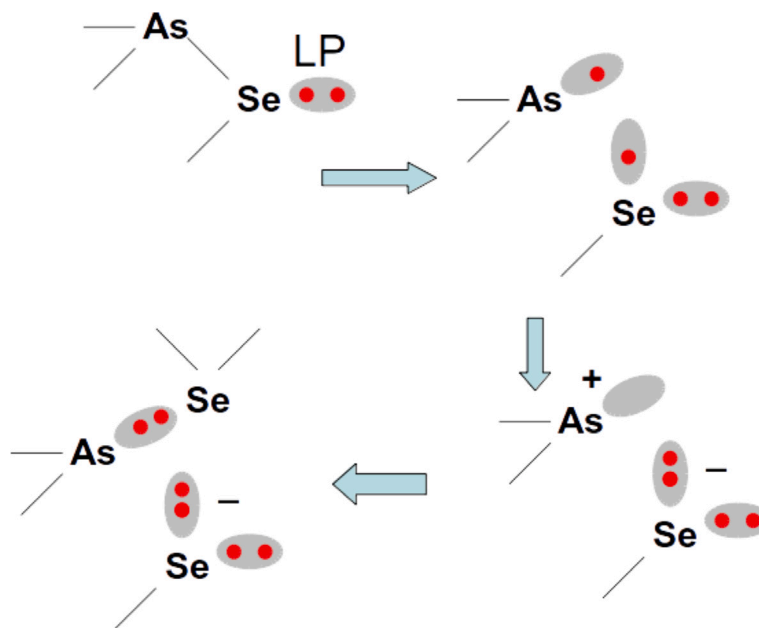

Fig. 11. Sketch of the formation of a Valence Alternation Pair (VAP) from undercoodinated As e Se atoms.

The fraction of Ge–As bonds is similar in Si–GAS and in the corresponding GAS alloy (with the same Se and As content). This might be surprising at first sight, since the overall fraction of Ge atoms is reduced in Si–GAS. However, also the Se atoms available to form Ge–Se bonds are reduced in the presence of Si because the Si-Se bonds are stronger and form more easily than Ge–Se bonds. This results in a similar fraction of Ge–As wrong bonds in Si–GAS and GAS with the same fraction of As and Se. Somehow, Si substitutes Ge that are already bound to Se only. Note that in the models of GAS and Si–GAS most of Ge–As bonds involve tetrahedral Ge atoms (see Table SVIII in the SM).

Regarding electronic properties, the optical Tauc gap and the electronic DOS (HSE functional) are compared with those of GAS alloys in Table 4 and Fig. 9. A zooming of the DOS close to the band gap with the IPR is reported in Fig. 17. The localized states in the gap do not involve Si atoms. The Si–X bonds are overall stronger than the others, and the corresponding states fall deep in the valence bands.

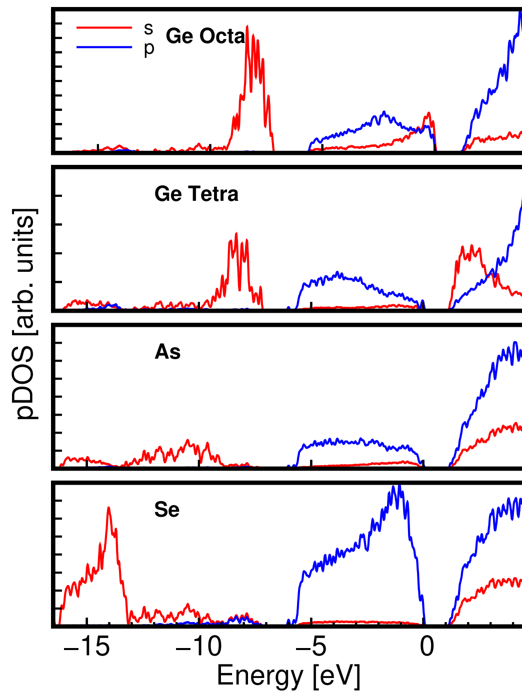

Fig. 12. Electronic density of states (HSE functional) of the mq120 model of a-$Ge_{15}As_{34}Se_{51}$ projected on different atomic *s* and *p* orbitals for the different atomic species. The contribution from *d* orbitals is negligible on the scale of the figure and it is omitted. The projections on Ge atoms are resolved for tetrahedral and defective octahedral-like/pyramidal configurations.

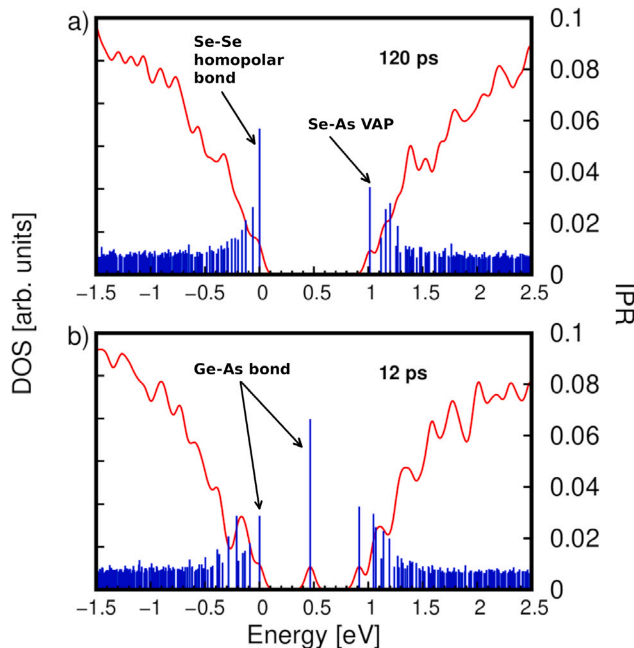

Fig. 13. A zooming of the DOS close to the band gap and the values of the Inverse Participation Ratio (IPR, right scale) are shown for the models of a-$Ge_{25}As_{30}Se_{45}$ quenched in (a) 120 and (b) 12 ps. The arrows indicate the characters of the most localized orbitals (HSE functional).

The states with a high IPR close to the edge and inside the gap are mostly localized on Ge–As and As–As wrong bonds as in previous GAS models. An example of such a state is shown in Fig. 17. The similar fraction of Ge–As wrong bonds in GAS and Si–GAS would lead

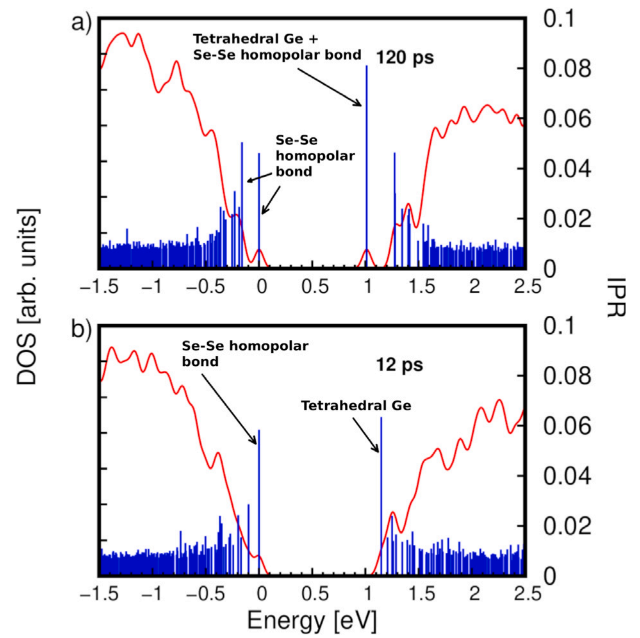

Fig. 14. A zooming of the DOS close to the band gap and the values of the Inverse Participation Ratio (IPR, right scale) are shown for the models of a-$Ge_{25}As_{10}Se_{65}$ quenched in (a) 120 and (b) 12 ps. The arrows indicate the characters of the most localized orbitals (HSE functional). The LUMO states of the mq120 and the mq12 models are localized on corner-sharing and isolated Ge tetrahedra, respectively.

Table 5
Partial coordination numbers and fraction of tetrahedral Ge atoms (Ge_t) in the $Si_{10}Ge_{15}As_{30}Se_{45}$ models generated with different quenching times.

Model	With	Si	Ge	As	Se	Total
$Si_{10}Ge_{15}As_{30}Se_{45}$ (120 ps) Ge_t 35%	Si	0.12	0.04	0.74	3.10	4.00
	Ge	0.03	0.16	0.65	2.52	3.36
	As	0.25	0.33	1.52	0.97	3.07
	Se	0.69	0.84	0.65	0.02	2.20
$Si_{10}Ge_{15}As_{30}Se_{45}$ (40 ps) Ge_t 28%	Si	0.08	0.12	0.76	3.04	4.00
	Ge	0.08	0.21	0.51	2.55	3.35
	As	0.25	0.25	1.51	1.03	3.05
	Se	0.68	0.85	0.69	0.02	2.23
$Si_{10}Ge_{15}As_{30}Se_{45}$ (12 ps) Ge_t 36%	Si	0.16	0.16	0.66	3.02	4.00
	Ge	0.11	0.13	0.60	2.59	3.43
	As	0.22	0.30	1.53	1.00	3.05
	Se	0.67	0.86	0.67	–	2.20

Table 6
Percentage of the different types of bonds in the models of $Si_{10}Ge_{15}As_{30}Se_{45}$ generated with different quenching time τ_q. The same values for $Ge_{25}As_{30}Se_{45}$ are also reported for the sake of comparison.

Composition	$Si_{10}Ge_{15}As_{30}Se_{45}$			$Ge_{25}As_{30}Se_{45}$		
τ_q (ps)	120	40	12	120	40	12
energy (meV/at.)	0	+10.7	+16.2	0	+8.3	+17.6
SiSe (%)	22	22	21	–	–	–
GeSe	27	27	27.5	49.5	50.5	47
AsSe	21	22	21	26	26	28
SiSi	0.4	0.3	0.6	–	–	–
AsAs	16	16	16	15	16	14
SiAs	5	5	5	–	–	–
GeAs	7	5	6	8	6	9
SeSe	0.3	0.3	–	–	0.7	0.7
SiGe	0.3	0.9	1.1	–	–	–
GeGe	0.9	1.1	0.7	1.4	0.5	1.9

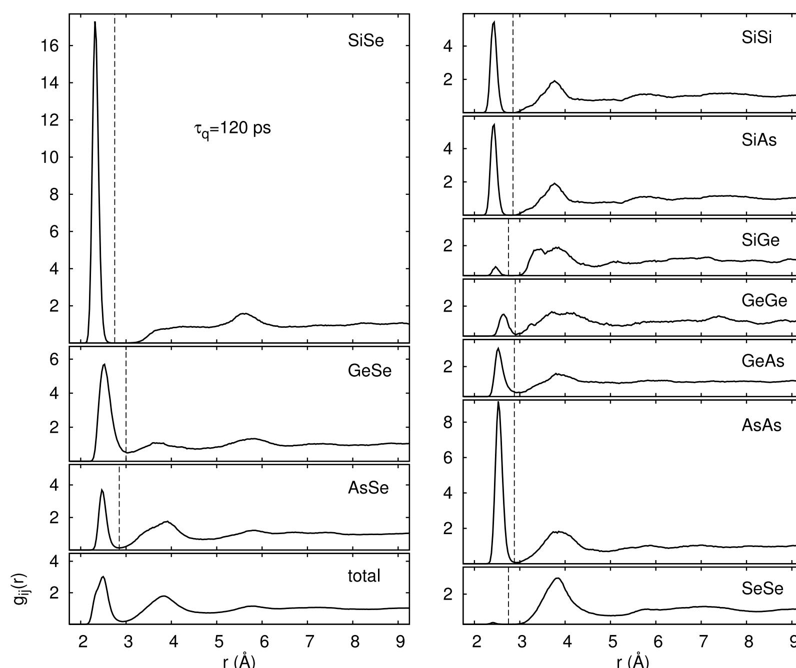

Fig. 15. Pair correlation functions of the mq120 model of $Si_{10}Ge_{15}As_{30}Se_{45}$.

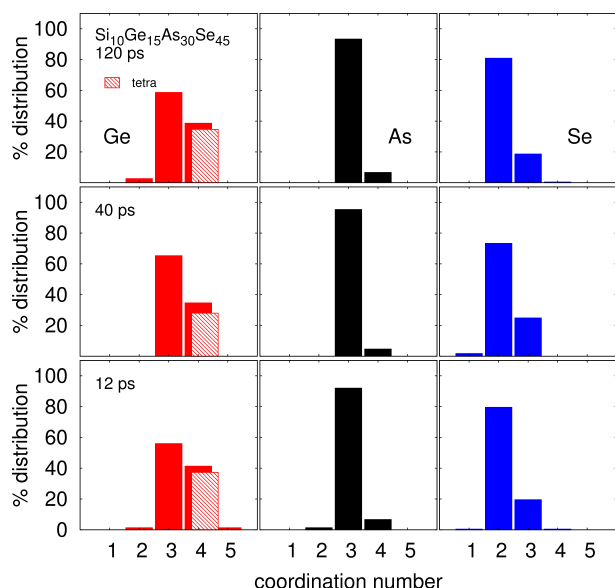

Fig. 16. Distribution of coordination numbers of the $Si_{10}Ge_{15}As_{30}Se_{45}$ models generated with different quenching times.

to a similar drift related to the removal of wrong bonds. However, the presence of Si would mitigate the drift anyway due to the reduction of Ge in octahedral/pyramidal-like configurations that would contribute to the drift via the octahedral → tetrahedral transformation.

In fact, as shown in Table 4, the fraction of tetrahedral Ge (over the total number of Ge atoms) is the same in Si–GAS and GAS (with the same As and Se content) implying a lower absolute number of octahedral/pyramidal configurations of Ge in Si–SAG.

As already mentioned, Ge–As bonds involve mostly tetrahedral Ge atoms. Therefore, the removal of Ge–As does not necessarily imply the removal of pyramids. The two sources of drift, pyramid to tetrahedral transformation and removal of wrong bonds, should actually operate in parallel.

The Tauc band gap is larger by 0.14 eV in the Si–GAS model than in the GAS model with the same As and Se content. The dependence of the Tauc gap on the quenching time is also similar in the two systems. Note that there is a pronounced Urbach tail in the conduction band of Si–GAS (Fig. 17) that extends much deeper in the gap than in the GAS model with the same fraction of As and Se. The states in the Urbach tail in the conduction band are localized mostly on Ge–As and As–As bonds as it occurs for the GAS model. We might conceive that these Ge–As states are more or less at the same position in energy in Si–GAS and GAS; the widening of the band gap in Si–GAS therefore brings into the gap region states localized on Ge–As bonds that were deeper in the conduction band in GAS; as a result, the conduction Urbach tail in Si–GAS is larger than in GAS.

6. Digression on the connection between drift and fragility

In this section, we discuss possible connections between wrong bonds and the two functional properties of the switching alloys we are interested in: the drift of the threshold voltage with time and the difference in threshold voltage between the first and second fire (forming).

In contrast to the results presented so far, the discussion in this section is more speculative. Here we would like to link the forming and drift phenomena to the fragility of the supercooled liquid in which the amorphous turns into during the switching and in particular during the transformation of the asdep material in the first fire.

According to the taxonomy introduced by Angell [91], supercooled liquids are classified as fragile or strong on the basis of the temperature dependence of their viscosity. An ideal strong liquid shows an Arrhenius behavior of the viscosity η from the melting temperature T_m down to the glass transition temperature T_g. On the contrary, in a fragile liquid a super-Arrhenius rise of η is observed by approaching T_g. The super-Arrhenius behavior is often described by a Vogel–Tammann–Fulcher (VTF) function $\eta = \eta_o \exp(\frac{E}{k_B(T-T_o)})$ with η_o, E and T_o as fitting parameters [91].

The degree of fragility is measured by the fragility index m defined by the logarithmic derivative of η at T_g, $m = d(log_{10}\eta)/d(T_g/T)\mid_{T=T_g}$.

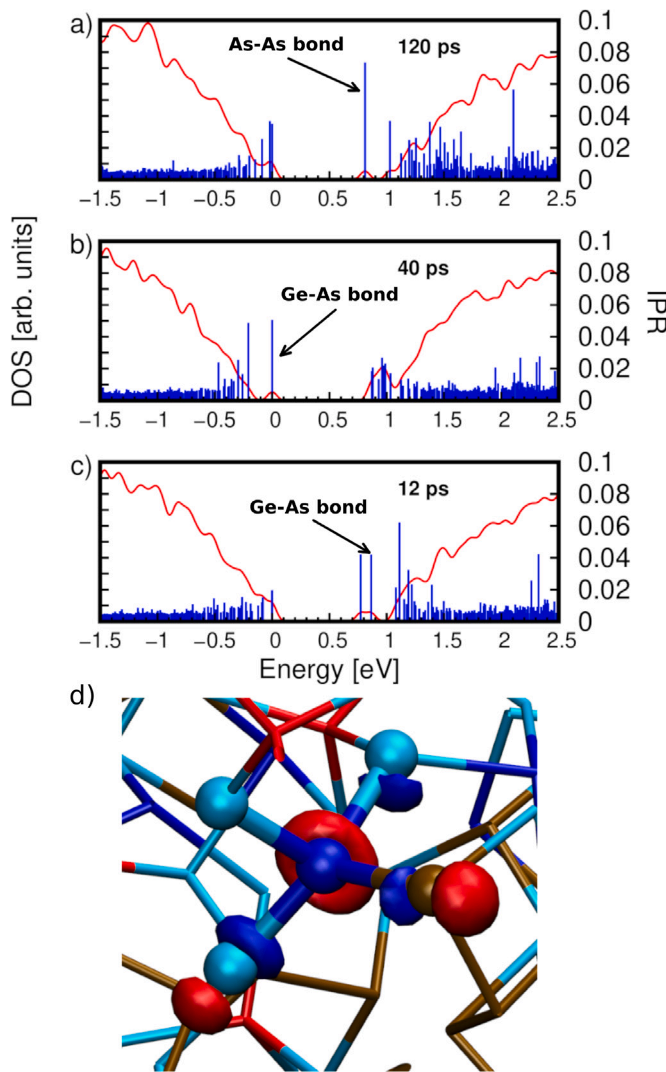

Fig. 17. (a)–(c) Zooming of the electronic DOS (HSE functional) and inverse participation ratio (IPR) of the $Si_{10}Ge_{15}As_{30}Se_{45}$ models generated with different quenching times. (d) Picture of the isosurfaces of the LUMO in the mq12 model. The LUMO is strongly localized on a Ge–As bond of a 4-coordinated Ge in a Ge–$AsSe_3$ configuration. Blue, azure and brown spheres denote Ge, Se and As atoms.

Silica and PVC are prototypical strong and fragile liquid with respectively $m = 15$ and $m = 195$. GeSeAs alloys are moderately fragile with m in the range 25–40 depending on composition [92].

It is known that the degree of fragility correlates with the extent of the structural relaxations of the glass below T_g [92]. This can be understood within the Adam-Gibbs [91] theory which relates the viscosity of the supercooled liquid with its configurational entropy S_c as $\eta = \eta_o \exp(\frac{C}{S_c T})$ where C is a constant. As discussed in Ref. [92], in the glass below T_g the mobility is low and the system is frozen in a configuration with $S_c(T_g)$. The continuation of the function $\eta(T)$ below T_g and the use of the Adam-Gibbs formula indicates, however, that an ideal glass with a configurational entropy $S_c(T)$ lower than $S_c(T_g)$ might actually exist. The difference between $S_c(T)$ and $S_c(T_g)$ is a driving force for structural relaxations that increases with the degree of fragility. Therefore, the higher the fragility in the supercooled liquid, the greater the extent of structural relaxation in the glass below T_g and thus the drift of several properties including eventually the threshold voltage. In addition, since a more fragile liquid is also more mobile just above T_g, we might expect that the rate of structural relaxation below T_g would also be larger. Therefore, not only the thermodynamical driving force (difference in entropy between actual and ideal glasses) but also the kinetics of structural relaxations is expected to be enhanced by a higher fragility.

Moreover, strong and fragile liquids are believed to display qualitative differences in the shape of the so called energy landscape [93]. In a strong liquid a single wide basin is present, which means that the properties of the glass are expected to be weakly dependent on the preparation conditions. In contrast, in a fragile liquid many deep minima are present separated by high energy barriers. During glass formation, the system can become trapped in one of the several deep minima without reaching the actual ideal glass. In such a system, the properties of the amorphous phase, including eventually the threshold voltage for switching, are more strongly dependent on the preparation conditions.

In the case of ovonic materials, we might conceive that the asdep phase is closer to the ideal glass than the amorphous phase generated during the forming. The difference between the two phases, including the threshold switching, is thus expected to be larger the higher is the fragility of the supercooled liquid. Therefore, we might conceive that a more fragile liquid would give rise to both a larger drift in V_T and a larger ΔV_T.

Regarding the dependence of the fragility of the liquid on the composition of the alloy, in Ref. [92] it is shown that the fragility is higher the larger is the deviation of composition from the pseudobinary line $(GeSe_2)_x(As_2Se_3)_{1-x}$. This deviation from stoichiometry was quantified by the quantity $\%/100 = (1\text{-}x\text{-}y)\text{-}2x\text{-}1.5y$ for the alloy with composition $Ge_xAs_ySe_{1-x-y}$; this quantity is zero when the Se atoms can exactly saturate the bonds with Ge in $GeSe_2$ and the bonds with As in As_2Se_3. The fragility index m is minimal at $\%/100 = 0$. This dependence of the m index on composition can be understood by considering that the fragility is controlled by two features: (i) the dimensionality of the structural organization in the liquid (1D molecular of chain-like, 2D planar-like, 3D connected network) and, within the same type of structural organization (1D, 2D or 3D), (ii) by the degree of structural heterogeneities. Note that the presence of Ge in the alloys is needed to turn the mostly 2D structure of As_2Se_3 into a 3D connected network and to reduce the fragility. At the same time, deviations from pseudobinary lines give rise to wrong bonds which represent a source of structural heterogeneity.

In our previous work on the binary chalcogenide GeTe, we have indeed demonstrated that the dynamical and structural heterogeneities of the supercooled liquid are linked with the presence of chains of Ge–Ge homopolar bonds [94]. A similar phenomenology might apply to the GeAsSe system. Therefore, we might envisage having a minimum in both the fraction of wrong bonds and the fragility for compositions along the pseudobinary lines $(GeSe_2)_x(As_2Se_3)_{1-x}$ and $(GeSe_4)_x(As_2Se_3)_{1-x}$ for which we would thus expect a lower drift in V_T and a smaller ΔV_T between the first and second fire. Moreover, since $GeTe_4$ is less fragile than $GeTe_2$ [95] one would also expect a lower fragility on the $(GeSe_4)_x(As_2Se_3)_{1-x}$ tie line.

7. Conclusions

In this work, we have generated amorphous models of GeAsSe alloys with different compositions by quenching from the melt by means of DFT molecular dynamics simulations. We considered first two Ge-doped As_2Se_3 systems, namely $Ge_{15}(As_2Se_3)_{17}$ and $Ge_{25}(As_2Se_3)_{15}$. These compositions are Se-poor as there are not enough Se atoms to form all the Ge–Se and As–Se bonds needed to saturate the valence of Ge and As atoms. Then we considered two compositions with the same 25% content of Ge that lie on the GeSe–As_2Se_3 or $GeSe_2$–As_2Se_3 pseudobinary lines. Finally, we considered a second composition along the $GeSe_2$–As_2Se_3 pseudobinary line with a lower Ge content of 12.5%.

The analysis of the models allowed us to characterize the bonding properties of the amorphous network. Atomic coordination mostly

obeys the $8 - N$ rule where N is the number of valence electrons, with Se 2-coordinated, As 3-coordinated and Ge 4-coordinated. The bonding of Se and As is due to the three p orbitals only, while 4-coordinated Ge atoms involve a sp^3 hybridization. However, a fraction of Se atoms are 3-coordinated due to the formation of dative bonds with 3-coordinated Ge atoms in pyramidal configurations forming bonds with p orbitals only. The majority of bonds are of the type As–Se and Ge–Se for all compositions. However, in the Se-poor alloys, a sizable fraction of As–As and Ge–As bonds is found. The latter can be seen as wrong bonds as they are weaker than the Ge–Se and As–Se bonds which are present in the binary systems $GeSe_x$ and As_2Se_3 the ternary alloys can be thought to originate from. For the same composition, we generated different models with different quenching times that display different stability (total energy). The models quenched more rapidly are less stable (higher total energy) and should be closer to the system after forming. The more stable model is, instead, closer to the asdep amorphous phase before forming. The less stable models have wider Urbach tails, a larger density of defect states in the gap and a smaller optical Tauc gap which are expected to lead to a lower threshold voltage according to the phenomenological models proposed in the literature. In the Se-poor alloys the in-gap states are localized on Ge–As bonds whose concentration increases by increasing the fraction of Ge. These alloys seem more sensitive to the quenching time and are thus expected to give rise to a stronger drift and a large difference in the threshold voltage between the first and second fire. Once the fraction of Se atoms is sufficient to saturate the bonds with Ge and As, the fraction of wrong bonds decreases leading to structures less sensitive to the quenching time. Getting rid of the Ge–As wrong bonds is thus the first requisite to have a low drifting material. However, a second possible source of drift is the transformation between pyramidal Ge and tetrahedral Ge, the latter being energetically more stable. Although this transformation does not seem to affect Urbach tails and in-gap states, they do lead to a widening of the optical Tauc gap as far as we can infer from the analysis of the $Ge_{12.5}As_{25}Se_{62.5}$ composition. The pyramids → tetrahedra transformation is possibly less severe than the structural relaxations involving Ge–As because the Ge–Se bonds are stronger than the Ge–As bonds and thus the activation energy to be overcome is possibly larger. This second source of drift can be mitigated by partially substituting Ge atoms with elements that do not form pyramids with Se but only tetrahedra such as Si but also Ga. A third source of structural relaxations is the transformation of edge-sharing into corner-sharing tetrahedra well documented in $GeSe_x$ alloys. This process is less severe in $GeSe_x$–As_2Se_3 alloy as the mixing with As_2Se_3 somehow dilutes the tetrahedra reducing the occurrence of edge-sharing configurations. Moreover, it is unknown whether this process would affect the electronic transport properties as no experimental nor theoretical data are available in this respect. We can summarize a few possible recipes to mitigate the drift in GeAsSe alloys: the drift is mostly due to Ge and thus minimizing the content of Ge is beneficial. Once the fraction of Ge is dictated by the required target on the glass transition temperature, it would be beneficial to have a Se content sufficiently high to saturate the bonds with As and Ge which would minimize the fraction of Ge–As wrong bonds. Partially substituting Ge with other elements forming only tetrahedra such as Si could minimize the drift associated with pyramids → tetrahedra transformation. Finally, alloying $GeSe_x$ with As_2Se_3 allows diluting the tetrahedra, thus reducing the fraction of edge-sharing configuration that would also lead to structural relaxations, although their impact on transport properties is currently unknown. As a final comment, we remark that our conclusions are based on the analysis of a very limited set of models. The simulations provided some hints on the behavior of these alloys which, however, must be confirmed by a more extensive analysis of the in-gap states in a large number of models to be generated by leveraging machine learning interatomic potentials as it has been recently done for telluride alloys [69].

CRediT authorship contribution statement

Sebastiano Caravati: Visualization, Validation, Software, Methodology, Investigation, Formal analysis, Data curation. **Dario Baratella:** Writing – review & editing, Visualization, Validation, Software, Methodology, Investigation, Formal analysis, Data curation. **Paolo Fantini:** Validation, Project administration, Funding acquisition, Conceptualization. **Marco Bernasconi:** Writing – original draft, Supervision, Funding acquisition, Formal analysis, Conceptualization.

Code availability

CP2k code is freely available at https://www.cp2k.org.

Declaration of competing interest

The authors declare that they have no known competing financial interests or personal relationships that could have appeared to influence the work reported in this paper.

Appendix A. Supplementary data

Supplementary material related to this article can be found online at https://doi.org/10.1016/j.solidstatesciences.2025.108127.

Data availability

Data will be made available on request.

References

[1] S.R. Ovshinki, Reversible electrical switching phenomena in disordered structures, Phys. Rev. Lett. 21 (1969) 1450–1453, http://dx.doi.org/10.1103/PhysRevLett.21.1450.

[2] M. Zhu, Z. Ren, K. Song, Ovonic threshold switching selectors for three-dimensional stackable phase-change memory, MRS Bull. 44 (2019) 715–720, http://dx.doi.org/10.1557/mrs.2019.206.

[3] Z. Zhao, S. Clima, D. Garbin, R. Degraeve, G. Pourtois, Z. Song, M. Zhu, Chalcogenide ovonic threshold switching selector, Nano-Micro Lett. 16 (2024) 81, http://dx.doi.org/10.1007/s40820-023-01289-x.

[4] P. Fantini, N. Polino, A. Ghetti, D. Ielmini, Threshold switching by bipolar avalanche multiplication in ovonic chalcogenide glasses, Adv. Elect. Mater. 9 (2023) 2300037, http://dx.doi.org/10.1002/aelm.202300037.

[5] M. Wuttig, N. Yamada, Phase-change materials for rewriteable data storage, Nat. Mater. 6 (2007) 824–832, http://dx.doi.org/10.1038/nmat2009, URL www.nature.com/naturematerials.

[6] W. Zhang, R. Mazzarello, M. Wuttig, E. Ma, Designing crystallization in phase-change materials for universal memory and neuro-inspired computing, Nat. Rev. Mater. 4 (2019) 150–168, http://dx.doi.org/10.1038/s41578-018-0076-x, URL https://www.osti.gov/biblio/1609476.

[7] P. Noé, C. Vallée, F. Hippert, F. Fillot, J.-Y. Raty, Phase-change materials for non-volatile memory devices: from technological challenges to materials science issues, Semicond. Sci. Technol. 33 (1) (2018) 013002, http://dx.doi.org/10.1088/1361-6641/AA7C25, URL https://iopscience.iop.org/article/10.1088/1361-6641/aa7c25 https://iopscience.iop.org/article/10.1088/1361-6641/aa7c25/meta.

[8] P. Fantini, Phase change memory applications: the history, the present and the future, J. Phys. D: Appl. Phys. 53 (2020) 283002, http://dx.doi.org/10.1088/1361-6463/ab83ba.

[9] P. Cappelletti, R. Annunziata, F. Arnaud, F. Disegni, A. Maurelli, P. Zuliani, Phase change memory for automotive grade embedded NVM applications, J. Phys. D: Appl. Phys. 53 (2020) 193002, http://dx.doi.org/10.1088/1361-6463/ab71aa.

[10] H.-Y. Cheng, F. Carta, W.C. Chien, H.-L. Lung, M.J. BrightSky, 3D cross-point phase-change memory for storage-class memory, J. Phys. D: Appl. Phys. 52 (2019) 473002, http://dx.doi.org/10.1088/1361-6463/ab39a0.

[11] D. Kau, S. Tang, I.V. Karpov, R. Dodge, B. Klehn, J.A. Kalb, J. Strand, A. Diaz, N. Leung, J. Wu, S. Lee, T. Langtry, K. Chang, C. Papagianni, J. Lee, J. Hirst, S. Erra, E. Flores, N. Righos, H. Castro, G. Spadini, A stackable cross point phase change memory, in: IEEE International Electron Devices Meeting, IEDM, 2009, pp. 1–4, http://dx.doi.org/10.1109/IEDM.2009.5424263.

[12] A. Fazio, Advanced technology and systems of cross point memory, in: IEEE International Electron Devices Meeting, IEDM, 2020, pp. 24.1.1–24.1.4, http://dx.doi.org/10.1109/IEDM13553.2020.9371976.

[13] M. Alayan, E. Vianello, G. Navarro, C. Carabasse, S. La Barbera, A. Verdy, N. Castellani, A. Levisse, G. Molas, L. Grenouillet, T. Magis, F. Aussenac, M. Bernard, B. DeSalvo, J.M. Portal, E. Nowak, In-depth investigation of programming and reading operations in RRAM cells integrated with ovonic threshold switching (OTS) selectors, in: IEEE International Electron Devices Meeting, IEDM, 2017, pp. 2.3.1–2.3.4, http://dx.doi.org/10.1109/IEDM.2017.8268311.

[14] S. Hong, H. Choi, J. Park, Y. Bae, K. Kim, W. Lee, S. Lee, H. Lee, S. Cho, J. Ahn, S. Kim, T. Kim, M.-H. Na, S. Cha, Extremely high performance, high density 20 nm self-selecting cross-point memory for compute express link, in: IEEE International Electron Devices Meeting, IEDM, 2022, pp. 18.6.1–18.6.4, http://dx.doi.org/10.1109/IEDM45625.2022.10019415.

[15] F. Pellizzer, A. Pirovano, R. Bez, R.L. Meyer, Status and perspectives of chalcogenide-based crosspoint memories, in: IEEE International Electron Devices Meeting, IEDM, 2023, pp. 1–4, http://dx.doi.org/10.1109/IEDM45741.2023.10413669.

[16] I.-M. Park, K.W. Lee, J.-H. Park, S.J. Song, T.Y. Kim, Z. Wu, W.J. Lee, B.D. Choi, Y.J. Jeong, S.C. Oh, K. Park, B.J. Kuh, Y.J. Song, Y.G. Shin, J.H. Song, Enhanced endurance characteristics in high performance 16 nm selector only memory (SOM), in: IEEE International Electron Devices Meeting, IEDM, 2023, pp. 1–4, http://dx.doi.org/10.1109/IEDM45741.2023.10413748.

[17] T. Ravsher, D. Garbin, A. Fantini, R. Degraeve, S. Clima, G.L. Donadio, Self-rectifying memory cell based on SiGeAsSe ovonic threshold switch, IEEE Trans. Electron Devices 70 (2023) 2276–2281, http://dx.doi.org/10.1109/TED.2023.3252491.

[18] P. Fantini, A. Ghetti, E. Varesi, A. Pirovano, F. Pellizzer, D. Baratella, C. Ribaldone, S. Caravati, D. Campi, M. Bernasconi, R. Bez, V_t window model of the single-chalcogenide xpoint memory (SXM), in: IEEE International Electron Devices Meeting, IEDM, San Francisco, CA, USA, 2024, pp. 1–4, http://dx.doi.org/10.1109/IEDM50854.2024.10873337.

[19] S. Clima, B. Govoreanu, K. Opsomer, A. Velea, N.S. Avasarala, W. Devulder, I. Shlyakhov, G. Donadio, T. Witters, S. Kundu, L. Goux, V. Afanasiev, G. Kar, G. Pourtois, Atomistic investigation of the electronic structure, thermal properties and conduction defects in Ge-rich Ge_xSe_{1-x} materials for selector applications, in: IEEE International Electron Devices Meeting, IEDM, 2017, pp. 4.1.1–4.1.4, http://dx.doi.org/10.1109/IEDM.2017.8268323.

[20] H. Cheng, W. Chien, I. Kuo, C. Yeh, L. Gignac, et al., Ultra-high endurance and low i_{OFF} selector based on AsSeGe chalcogenides for wide memory window 3D stackable crosspoint memory, in: IEEE International Electron Devices Meeting, IEDM, 2018, pp. 37.3.1–37.3.4, http://dx.doi.org/10.1109/IEDM.2018.8614580.

[21] H. Cheng, W. Chien, I. Kuo, C. Yang, Y. Chou, et al., Optimizing AsSeGe chalcogenides by dopants for extremely low i_{OFF}, high endurance and low vth drift 3D crosspoint memory, in: IEEE International Electron Devices Meeting, IEDM, 2021, pp. 28.6.1–28.6.4, http://dx.doi.org/10.1109/IEDM19574.2021.9720704.

[22] H.Y. Cheng, W.C. Chien, I.T. Kuo, C.H. Yang, Y.C. Chou, R.L. Bruce, E.K. Lai, D. Daudelin, C.W. Yeh, L. Gignac, C.W. Cheng, A. Grun, C. Lavoie, N. Gong, L. Buzi, H.Y. Ho, A. Ray, H. Utomo, M. BrightSky, H.L. Lung, Optimizing assege chalcogenides by dopants for extremely low ioff, high endurance and low vth drift 3d crosspoint memory, in: IEEE International Electron Devices Meeting, IEDM, 2021, pp. 28.6.1–28.6.4, http://dx.doi.org/10.1109/IEDM19574.2021.9720704.

[23] P. Fantini, K.-W. Chang, Chalcogenide glass composition and chalcogenide switch devices, 2016, US Patent No. US 9379321 B1.

[24] I. Kaban, P. Jóvári, R. Wang, B. Luther-Davies, N. Mattern, J. Eckert, Structural investigations of $Ge_5As_xSe_{95-x}$ and $Ge_{15}As_xSe_{85-x}$ glasses using x-ray diffraction and extended x-ray fine structure spectroscopy, J. Phys.: Condens. Matter. 24 (38) (2012) 385802, http://dx.doi.org/10.1088/0953-8984/24/38/385802.

[25] I. Pethes, R. Chahal, V. Nazabal, C. Prestipino, A. Trapananti, S. Michalik, P. Jóvári, Chemical short-range order in selenide and telluride glasses, J. Phys. Chem. B 120 (2016) 9204–9214, http://dx.doi.org/10.1021/acs.jpcb.6b05996.

[26] Z. Černošek, E. Černošková, E. Todorov, J. Holubová, $Ge_{30}As_xSe_{70-x}$ bulk glasses from the point of view of chemistry, J. Solid State Chem. 291 (2020) 121599, http://dx.doi.org/10.1016/j.jssc.2020.121599.

[27] A. Stronski, T. Kavetskyy, L. Revutska, K. Shportko, M. Popovych, I. Kaban, P. Jóvári, Structural order in $(As_2Se_3)_x(GeS_2)_{1-x}$ glasses, J. Non-Cryst. Solids 572 (2021) 121075, http://dx.doi.org/10.1016/j.jnoncrysol.2021.121075.

[28] I. Pethes, I. Kaban, R.-P. Wang, B. Luther-Davies, P. Jóvári, Short range order in Ge–As–Se glasses, J. Alloys Compd. 623 (2015) 454–459, http://dx.doi.org/10.1016/j.jallcom.2014.11.002.

[29] M. Micoulaut, I. Pethes, P. Jóvári, L. Pusztai, M. Krbal, T. Wágner, V. Prokop, S. Michalik, K. Ikeda, I. Kaban, Structural properties of chalcogenide glasses and the isocoordination rule: Disentangling effects from chemistry and network topology, Phys. Rev. B 106 (2022) 014206, http://dx.doi.org/10.1103/PhysRevB.106.014206.

[30] G. Opletal, D.W. Drumm, T.C. Petersen, R.P. Wang, S.P. Russo, Ab initio comparison of bonding environments and threshold behavior in $Ge_xAs_{10}Se_{90--x}$ and $Ge_xSb_{10}Se_{90--x}$ glass models, J. Phys. Chem. A 119 (24) (2015) 6421–6427, http://dx.doi.org/10.1021/acs.jpca.5b00039.

[31] G. Opletal, R. Wang, S. Russo, Bonding trends within ternary isocoordinate chalcogenide glasses GeAsSe, Phys. Chem. Chem. Phys. 15 (2013) 4582–4588, http://dx.doi.org/10.1039/C3CP43364A.

[32] G. Opletal, D.W. Drumm, R.P. Wang, S.P. Russo, Structural modeling of $Ge_{6.25}As_{32.5}Se_{61.25}$ using a combination of reverse Monte Carlo and Ab initio molecular dynamics, J. Phys. Chem. A 118 (26) (2014) 4790–4796, http://dx.doi.org/10.1021/jp5017856.

[33] G. Opletal, R. Wang, S. Russo, Investigation of bonding within ab-initio models of geasse glasses, Chem. Phys. Lett. 575 (2013) 97, http://dx.doi.org/10.1016/j.cplett.2013.05.025.

[34] M. Xu, M. Xu, X. Miao, Deep machine learning unravels the structural origin of mid-gap states in chalcogenide glass for high-density memory integration, InfoMat 4 (2022) e12315, http://dx.doi.org/10.1002/inf2.12315.

[35] H.-J. Sung, M. Choi, Y. Kang, K. Yang, B. Koo, W. Zhe, H. Chae, C.S. Lee, Ab-initio screening of amorphous chalcogenides for selector-only memory (SOM) through electrical properties and device reliability, in: IEEE International Electron Devices Meeting, IEDM, 2024, pp. 1–4, http://dx.doi.org/10.1109/IEDM50854.2024.10873326.

[36] H.-J. Sung, M. Choi, Z. Wu, H. Chae, S. Heo, Y. Kang, B. Koo, J.-B. Park, W. Yang, Y. Park, Y. Ham, K. Yang, C.C. Lee, Microscopic origin of polarity-dependent V_{TH} shift in amorphous chalcogenides for 3D self-selecting memory, Adv. Sci. 11 (2024) 2408028, http://dx.doi.org/10.1002/advs.202408028.

[37] B. Cai, X. Zhang, D.A. Drabold, Building block modeling technique: Application to ternary chalcogenide glasses g-$Ge_2As_4Se_4$ and g-$AsGe_{0.8}Se_{0.8}$, Phys. Rev. B 83 (2011) 092202, http://dx.doi.org/10.1103/PhysRevB.83.092202.

[38] D. Adler, M.S. Shur, M. Silver, S.R. Ovshinsky, Threshold switching in chalcogenide-glass thin films, J. Appl. Phys. 51 (1980) 3289, http://dx.doi.org/10.1063/1.328036.

[39] A. Pirovano, A.L. Lacaita, A. Benvenuti, F. Pellizzer, R. Bez, Electronic switching in phase-change memories, IEEE Trans. Electron. Dev. 51 (2004) 452, http://dx.doi.org/10.1109/TED.2003.823243.

[40] A. Redaelli, A. Pirovano, A. Benvenuti, A.L. Lacaita, Threshold switching and phase transition numerical models for phase change memory simulations, J. Appl. Phys. 103 (2008) 111101, http://dx.doi.org/10.1063/1.2931951.

[41] D. Ielmini, Threshold switching mechanism by high-field energy gain in the hopping transport of chalcogenide glasses, Phys. Rev. B 78 (2008) 035308, http://dx.doi.org/10.1103/PhysRevB.78.035308.

[42] E. Piccinini, A. Cappelli, F. Buscemi, R. Brunetti, D. Ielmini, M. Rudan, C. Jacoboni, Hot-carrier trap-limited transport in switching chalcogenides, J. Appl. Phys. 112 (2012) 083722, http://dx.doi.org/10.1063/1.4761997.

[43] P. Fantini, S. Brazzelli, E. Cazzini, A. Mani, Band gap widening with time induced by structural relaxation in amorphous $Ge_2Sb_2Te_5$ films, Appl. Phys. Lett. 100 (2012) 013505, http://dx.doi.org/10.1063/1.3674311.

[44] D. Ielmini, A.L. Lacaita, D. Mantegazza, Recovery and drift dynamics of resistance and threshold voltages in phase-change memories, IEEE Trans. Electron Devices 54 (2007) 308–315, http://dx.doi.org/10.1109/TED.2006.888752.

[45] W. Zhang, E. Ma, Unveiling the structural origin to control resistance drift in phase-change memory materials, Mater. Today 41 (2020) 156, http://dx.doi.org/10.1016/j.mattod.2020.07.016.

[46] N. Ciocchini, M. Cassinerio, D. Fugazza, D. Ielmini, Modeling of threshold-voltage drift in phase-change memory (PCM) devices, IEEE Trans. Electron Devices 59 (2012) 3084–3090, http://dx.doi.org/10.1063/1.3599559.

[47] D. Ielmini, Y. Zhang, Analytical model for subthreshold conduction and threshold switching in chalcogenide-based memory devices, J. Appl. Phys. 102 (2007) 054517, http://dx.doi.org/10.1063/1.2773688.

[48] S. Ban, J. Lee, Y. Seo, W. Lee, T. Kim, H. Hwang, Advances in ovonic threshold switch selector technologies for storage class memory: From fundamentals to development and beyond, Adv. Electron. Mater. 11 (2025) 2400665, http://dx.doi.org/10.1002/aelm.202400665.

[49] Z. Chen, L. Wang, W. Cheng, H. Tong, X. Miao, Controllable on-resistance and its thermal-induced channel expansive model in ovonic threshold switch selector, IEEE Trans. Elect. Dev. 70 (2023) 366–370, http://dx.doi.org/10.1109/TED.2022.3224702.

[50] A. Boniardi, D. Ielmini, Physical origin of the resistance drift exponent in amorphous phase change materials, Appl. Phys. Lett. 98 (2011) 243506, http://dx.doi.org/10.1063/1.3599559.

[51] M. Rizzi, A. Spessot, P. Fantini, D. Ielmini, Role of mechanical stress in the resistance drift of $Ge_2Sb_2Te_5$ films and phase change memories, Appl. Phys. Lett. 99 (2007) 223513, http://dx.doi.org/10.1063/1.3664631.

[52] T.D. Kühne, M. Krack, F.R. Mohamed, M. Parrinello, Efficient and accurate Car-Parrinello-like approach to Born-Oppenheimer molecular dynamics, Phys. Rev. Lett. 98 (2007) 066401, http://dx.doi.org/10.1103/PhysRevLett.98.066401.

[53] M. Krack, M. Parrinello, Quickstep: Make the atoms dance, High Perform. Comput. Chem. NIC 25 (2004) 29–51.

[54] J. Vandevondele, M. Krack, F. Mohamed, M. Parrinello, T. Chassaing, J. Hutter, Quickstep: Fast and accurate density functional calculations using a mixed Gaussian and plane waves approach, Comput. Phys. Comm. 167 (2005) 103–128, http://dx.doi.org/10.1016/j.cpc.2004.12.014.www.cp2k.org.

[55] A.D. Becke, Density-functional exchange-energy approximation with correct asymptotic behavior, Phys. Rev. A 38 (1988) 3098–3100, http://dx.doi.org/10.1103/PhysRevA.38.3098.

[56] C. Lee, W. Yang, R.G. Parr, Development of the Colle–Salvetti correlation-energy formula into a functional of the electron density, Phys. Rev. B 37 (1988) 785, http://dx.doi.org/10.1103/PhysRevB.37.785.

[57] M. Micoulaut, R. Vuilleumier, C. Massobrio, Improved modeling of liquid $gese_2$: Impact of the exchange–correlation functional, Phys. Rev. B 79 (2009) 214205, http://dx.doi.org/10.1103/PhysRevB.79.214205.

[58] S.L. Roux, A. Bouzid, M. Boero, C. Massobrio, The structure of liquid GeSe revisited: A first principles molecular dynamics study, J. Chem. Phys. 138 (2013) 174505, http://dx.doi.org/10.1063/1.4803115.

[59] J.P. Perdew, K. Burke, M. Ernzerhof, Generalized gradient approximation made simple, Phys. Rev. Lett. 77 (1996) 3865, http://dx.doi.org/10.1103/PhysRevLett.77.3865.

[60] S. Goedecker, M. Teter, J. Hutter, Separable dual-space Gaussian pseudopotentials, Phys. Rev. B 54 (1996) 1703, http://dx.doi.org/10.1103/PhysRevB.54.1703.

[61] S. Caravati, M. Bernasconi, T.D. Kühne, M. Krack, M. Parrinello, Coexistence of tetrahedral- and octahedral-like sites in amorphous phase change materials, Appl. Phys. Lett. 91 (2007) 171906, http://dx.doi.org/10.1063/1.2801626.

[62] E. Spreafico, S. Caravati, M. Bernasconi, First-principles study of liquid and amorphous $InGeTe_2$, Phys. Rev. B 83 (2011) 144205, http://dx.doi.org/10.1103/PhysRevB.83.144205.

[63] D. Acharya, O. Abou El Kheir, D. Campi, M. Bernasconi, Crystallization kinetics of nanoconfined GeTe slabs in GeTe/$TiTe_2$-like superlattices for phase change memories, Sci. Rep. 14 (2024) 3224, http://dx.doi.org/10.1038/s41598-024-53192-z.

[64] D. Acharya, O. Abou El Kheir, S. Marcorini, M. Bernasconi, Simulation of the crystallization kinetics of $Ge_2Sb_2Te_5$ nanoconfined in superlattice geometries for phase change memories, Nanoscale 17 (2025) 13828–13841, http://dx.doi.org/10.1039/d5nr00283d.

[65] S. Grimme, Semiempirical GGA-type density functional constructed with a long-range dispersion correction, J. Comput. Chem. 27 (2006) 1787–1799, http://dx.doi.org/10.1002/jcc.20495.

[66] P.L. Silvestrelli, E. Martin, M. Boero, A. Bouzid, G. Ori, C. Massobrio, Atomic structure of glassy $GeTe_4$ as a playground to assess the performances of density functional schemes accounting for dispersion forces, J. Phys. Chem. B 124 (2020) 11273–11279, http://dx.doi.org/10.1021/acs.jpcb.0c08628.

[67] C. Massobrio, E. Martin, Z. Chaker, M. Boero, A. Bouzid, S. LeRoux, G. Ori, Sensitivity to dispersion forces in first-principles modeling of disordered chalcogenides, Front. Mater. 5 (2018) 78, http://dx.doi.org/10.3389/fmats.2018.00078.

[68] R.P. Wang, A. Smith, B. Luther-Davies, H. Kokkonen, I. Jackson, Observation of two elastic thresholds in $Ge_xAs_ySe_{1-x-y}$ glasses, J. Appl. Phys. 105 (2013) http://dx.doi.org/10.1063/1.3079806.

[69] K. Konstantinou, S.R. Elliott, Atomistic modeling of charge-trapping defects in amorphous Ge-Sb-Te phase-change memory materials, Phys. Status Solidi RRL 17 (2023) 2200496, http://dx.doi.org/10.1002/pssr.202200496.

[70] J. Tauc, R. Grigorovici, A. Vancu, Optical properties and electronic structure of amorphous germanium, Phys. Status Solidi b 15 (1966) 627–637, http://dx.doi.org/10.1002/pssb.19660150224.

[71] A.V. Krukau, O.A. Vydrov, A.F. Izmaylov, G.E. Scuseria, Influence of the exchange screening parameter on the performance of screened hybrid functionals, J. Chem. Phys. 125 (2006) 224106, http://dx.doi.org/10.1063/1.2404663.

[72] S. Caravati, M. Bernasconi, T.D. Kühne, M. Krack, M. Parrinello, First-principles study of crystalline and amorphous $Ge_2Sb_2Te_5$ and the effects of stoichiometric defects, J. Phys.: Condens. Matter. 21 (2010) http://dx.doi.org/10.1088/0953-8984/22/39/399801.

[73] S. Caravati, M. Bernasconi, M. Parrinello, First principles study of the optical contrast in phase change materials, J. Phys.: Condens. Matter. 22 (2010) 315801, http://dx.doi.org/10.1088/0953-8984/22/31/315801.

[74] D.D. Vaughn, R.J. Patel, M.A. Hickner, R.E. Schaak, Single-crystal colloidal nanosheets of GeS and GeSe, J. Am. Chem. Soc. 132 (2010) 15170, http://dx.doi.org/10.1021/ja107520b.

[75] G. Dittmar, H. Schaefer, Die kristallstruktur von germaniumdiselenid, Acta Crystallogr. B 32 (1976) 2726, http://dx.doi.org/10.1107/S0567740876008704.

[76] K. Shimakawa, On the compositional dependence of the optical gap in amorphous semiconducting alloys, J. Non-Cryst. Solids 43 (1981) 229, http://dx.doi.org/10.1016/0022-3093(81)90119-8.

[77] A. Stergiou, P. Rentzeperis, The crystal structure of arsenic selenide, As_2Se_3, Z. Fuer Krist. 173 (1985) 185–191, http://dx.doi.org/10.1524/zkri.1985.173.3-4.185.

[78] N. Marzari, D. Vanderbilt, Maximally localized generalized Wannier functions for composite energy bands, Phys. Rev. B 56 (1997) 12847, http://dx.doi.org/10.1103/PhysRevB.56.12847.

[79] M. Wuttig, V. Deringer, X. Gonze, C. Bichara, J.-Y. Raty, Incipient metals: Functional materials with a unique bonding mechanism, Adv. Mater. 30 (2018) 1803777, http://dx.doi.org/10.1002/adma.201803777.

[80] G.C. Sosso, S. Caravati, R. Mazzarello, M. Bernasconi, Raman spectra of cubic and amorphous $Ge_2Sb_2Te_5$ from first principles, Phys. Rev. B 83 (2011) 134201, http://dx.doi.org/10.1103/PhysRevB.83.134201.

[81] D. Lencer, M. Salinga, M. Wuttig, Design rules for phase-change materials in data storage applications, Adv. Mat. 23 (2011) 2030, http://dx.doi.org/10.1002/adma.201004255.

[82] M. Xu, Y.Q. Cheng, H.W. Sheng, E. Ma, Nature of atomic bonding and atomic structure in the phase-change $Ge_2Sb_2Te_5$ glass, Phys. Rev. Lett. 103 (2009) 195502, http://dx.doi.org/10.1103/PhysRevLett.103.195502.

[83] J.R. Errington, P.G. Debenedetti, Relationship between structural order and the anomalies of liquid water, Nature 409 (2001) 318, http://dx.doi.org/10.1038/35053024.

[84] T.G. Edwards, S. Sen, Structure and relaxation in germanium selenide glasses and supercooled liquids: A raman spectroscopic study, J. Phys. Chem B 115 (2011) 4307, http://dx.doi.org/10.1021/jp202174x.

[85] A. Bouzid, G. Ori, M. Boero, E. Lampin, C. Massobrio, Atomic-scale structure of the glassy $Ge_2Sb_2Te_5$ phase change material: A quantitative assessment via first-principles molecular dynamics, Phys. Rev. B 96 (2017) 224204, http://dx.doi.org/10.1103/PhysRevB.96.224204.

[86] M. Ghayebloo, M. Rezvani, M. Tavoosi, The relationship between structural and optical properties of Se-Ge-As glasses, Infrared Phys. Techn. 90 (2018) 40–47, http://dx.doi.org/10.1016/j.infrared.2018.02.004.

[87] Y. Li, H. Wang, M. Shao, Y. Wang, S. Song, Y. Xue, Z. Song, Modulation of GeSe and As_2Se_3 motifs to optimise GeAsSe OTS performance and its mechanism, J. Mater. Chem. C 13 (2025) 735, http://dx.doi.org/10.1039/d4tc03586k.

[88] M. Kastner, D. Adler, H. Fritzsche, Valence-alternation model for localized gap states in lone-pair semiconductors, Phys. Rev. Lett. 37 (1976) http://dx.doi.org/10.1103/PhysRevLett.37.1504.

[89] J. Li, D.A. Drabold, Direct calculation of light-induced structural change and diffusive motion in glassy As_2Se_3, Phys. Rev. Lett. 85 (2000) 2785–2788, http://dx.doi.org/10.1103/PhysRevLett.85.2785.

[90] A. Slassi, L.-S. Medondjio, A. Padovani, F. Tavanti, X. He, S. Clima, D. Garbin, B. Kaczer, L. Larcher, P. Ordejón, A. Calzolari, Device-to-materials pathway for electron traps detection in amorphous GeSe-Based Selectors, Adv. Electron. Mater. 23 (2024) 2201224.

[91] C.A. Angell, Formation of glasses from liquids and biopolymers, Science 267 (1995) 1924, http://dx.doi.org/10.1126/science.267.5206.1924.

[92] T. Wang, O. Gulbiten, R. Wang, Z. Yang, A. Smith, B. Luther-Davies, P. Lucas, Relative contribution of stoichiometry and mean coordination to the fragility of Ge–As–Se glass forming liquids, J. Phys. Chem. B 118 (2014) 1436, http://dx.doi.org/10.1021/jp412226w.

[93] P.G. Debenedetti, F.H. Stillinger, Supercooled liquids and the glass transition, Nature 410 (2010) 259, http://dx.doi.org/10.1038/35065704.

[94] G.C. Sosso, J. Colombo, J. Behler, E. Del Gado, M. Bernasconi, Dynamical heterogeneities in the supercooled liquid state of the phase change compound GeTe, J. Phys. Chem. B 118 (2014) 13621, http://dx.doi.org/10.1021/jp507361f.

[95] R. Bhageria, K. Gunasekera, P. Boolchand, M. Micoulaut, Fragility and molar volumes of non-stoichiometric chalcogenides: The crucial role of melt/glass homogenization, Phys. Status Solidi b 251 (2014) 1322, http://dx.doi.org/10.1002/pssb.201350165.